Research Square

Preprints are preliminary reports that have not undergone peer review.
They should not be considered conclusive, used to inform clinical practice,
or referenced by the media as validated information.

# Multi-omics analysis reveals tissue-specific patterns of chicken growth driven by metabolic reorganization

**Vladimir Kaplan**

kaplanrimi@gmail.com

Sirius University of Science and Technology

**Mikhail Kulyashov**

Sirius University of Science and Technology

**Ivan Yevshin**

Sirius University of Science and Technology

**Nataliya Osik**

International Tomography Center

**Lyudmila Yanshole**

International Tomography Center

**Elena Shagimardanova**

Skolkovo Institute of Science and Technology

**Natalia Volkova**

Federal Scientific Center for Animal Husbandry named after Academician L.K. Ernst

**Anastasia Vetokh**

Federal Scientific Center for Animal Husbandry named after Academician L.K. Ernst

**Yuri Tsentalovich**

International Tomography Center

**Oleg Gusev**

Juntendo University

**Fedor Kolpakov**

Sirius University of Science and Technology

**Ilya Akberdin**

Sirius University of Science and Technology

---

**Article**

**Keywords:**

**Posted Date:** May 8th, 2026

**DOI:** https://doi.org/10.21203/rs.3.rs-9275884/v1

**License:** This work is licensed under a Creative Commons Attribution 4.0 International License.
Read Full License

**Additional Declarations:** No competing interests reported.

---

**Version of Record:** A version of this preprint was published at Scientific Reports on October 7th, 2026.
See the published version at https://doi.org/10.1038/s41598-026-73987-6.

# Multi-omics analysis reveals tissue-specific patterns of chicken growth driven by metabolic reorganization

**Vladimir Kaplan[1,*], Mikhail Kulyashov[1], Ivan Yevshin[1,2], Nataliya Osik[3], Lyudmila Yanshole[3], Elena Shagimardanova[4], Natalia Volkova[5], Anastasia Vetokh[5], Yuri Tsentalovich[3], Oleg Gusev[6,7,*], Fedor Kolpakov[1], and Ilya Akberdin[1,*]**

[1]Sirius University of Science and Technology, Sirius, 354340, Russia
[2]Biosoft.Ru, LLC., Novosibirsk, 630058, Russian Federation
[3]International Tomography Center SB RAS, Institutskaya str. 3a, Novosibirsk, 630090, Russia
[4]Genomics and Bioimaging Core Facility, Skolkovo Institute of Science and Technology, Moscow, 143026, Russia
[5]L. K. Ernst Federal Research Center for Animal Husbandry, Dubrovitsy, Podolsk, Moscow Oblast, 142132, Russia
[6]Intractable Disease Research Center, Graduate School of Medicine, Juntendo University, Tokyo, 113-8421, Japan
[7]Institute of Biochemistry and Genetics, Ufa Federal Research Centre of the Russian Academy of Sciences (IBG UFRC RAS), Ufa, 450054, Russia
[*]Corresponding authors: kaplanrimi@gmail.com (V.K.); o.gusev.fo@juntendo.ac.jp (O.G.); akberdinir@gmail.com (I.A.)

## ABSTRACT

Genetic variation in growth rate is associated with substantial metabolic differences in poultry, but its tissue-specific effects remain insufficiently characterized. Using an F2 population derived from Russian Snow White and White Cornish chickens, we profiled liver, leg muscle, and breast muscle from fast-growing (FG) and slow-growing (SG) birds using NMR metabolomics and CAGE-seq transcriptomics. These data were integrated into a refined genome-scale metabolic model using a Differential Pathway Flux Analysis (DPFA) framework.

Across tissues, FG birds showed coordinated but tissue-specific metabolic changes. Oxidative phosphorylation was reduced in both breast muscle and liver. Breast muscle exhibited selective redistribution within amino acid metabolism alongside suppressed folate pathways, while liver showed markedly elevated central carbon metabolism with concurrent suppression of amino acid and folate catabolism. In contrast, leg muscle demonstrated enhanced TCA cycle activity and nitrogen disposal, with reduced folate metabolism and broadly suppressed amino acid catabolism.

Transcriptomic analysis identified enrichment of hypoxia-related pathways and Wnt signaling in muscle tissues, along with coordinated downregulation of cell cycle–associated transcriptional programs, consistent with a shift toward hypertrophic growth.

These results were consistent across flux predictions, metabolomics, and transcriptomics, and provide a systems-level characterization of metabolic differences associated with growth rate in poultry.

## Introduction

Systems biology encompasses a range of approaches for studying complex biological systems, from cells to whole organisms, by analysing interactions among their components, including genes, proteins, and metabolites. It combines experimental biology with mathematical and computational methods to investigate emergent properties of systems rather than individual parts[1,2]. Metabolism, as a tightly interconnected network, is shaped by multiple biological hierarchies-genome, transcriptome, proteome-and by environmental factors[3].

Constraint-based analysis is applied to genome-scale models (GSM) in order to predict metabolic activity. This approach uses mathematical constraints and optimisation methods, such as flux balance analysis, to simulate metabolic states without requiring kinetic parameters. These models are mathematically reconstructed from genome annotations and include all known metabolic reactions linked to annotated genes. They capture metabolite-reaction relationships via a stoichiometric matrix under the assumption steady-state, whereby intracellular metabolite concentrations remain constant[4]. Incorporating omics data refines GSMs into context-specific (CS-GSM) models[5]. This constrains the solution space to active pathways and improves the prediction of tissue- or condition-specific metabolic activity. These models have been used to identify the effects of genetic or environmental changes on growth and yield in plants and animals.

The domestic chicken (*Gallus gallus*) is a key agricultural species for producing meat and eggs. Despite its economic importance, chicken metabolism remains incompletely characterised, and intensive selection for production traits has been

consistently associated with metabolic disorders, including sudden death syndrome, ascites, cardiovascular dysfunction, and muscle myopathies in broilers, as well as fatty liver disease in high-producing layer lines[6–9]. To address this knowledge gap, we analysed second-generation (F2) cross individuals of Russian Snow White (egg-laying) and White Cornish (meat-oriented) breeds, which differ markedly in growth rate but have a similar genetic background. This design reduces confounding genomic variation and enables metabolic differences to be more directly attributed to growth-related traits.

Beyond cellular metabolism, modern broilers exhibit behavioural and physiological characteristics of increased metabolic heat production and limited thermotolerance, most notably panting (hyperventilation), reduced performance in hot conditions, and greater susceptibility to heat stress, compared with layer breeds[10,11]. Recent genotype-comparison studies confirm that fast-growing birds suffer disproportionate performance and carcass-quality losses under thermal challenge relative to slower-growing lines[12,13]. Rapid, selection-driven growth also predisposes broilers to hypoxaemia and pulmonary hypertension/ascites under high oxygen demand[14], while at the tissue level, breast muscle hypertrophy can outpace capillary development, creating localised hypoxia through HIF-1-mediated pathways and contributing to myopathies such as wooden breast[15]. These population- and tissue-level observations are consistent with increased systemic energetic demand and elevated oxygen utilisation in fast-growing birds. However, accumulating evidence suggests that this demand is met through tissue-specific metabolic strategies rather than a uniform upregulation of mitochondrial oxidative phosphorylation across all organs. In breast muscle, modern broilers exhibit mitochondrial dysfunction, impaired OXPHOS complex activity, and a shift toward glycolytic metabolism under hypoxic conditions[16,17]; in liver, genotype-dependent differences in lipid metabolism and *de novo* fatty acid synthesis have been reported[18]; and across skeletal muscles, distinct fibre types display markedly different mitochondrial contents and respiratory capacities[19]. Taken together, these findings indicate that the metabolic costs of rapid growth are distributed non-uniformly across tissues.

Consistent with these observations, physiological and biochemical studies have shown that selection for rapid growth imposes non-uniform metabolic demands across tissues, leading to hierarchical allocation of nutrients and metabolic resources rather than a global increase in metabolic activity[8,20]. Breast muscle, which consists predominantly of fast-twitch glycolytic fibres across both fast- and slow-growing chicken lines, represents the primary site of hypertrophic growth in broilers and is particularly sensitive to anabolic regulation via amino acid availability and protein turnover[21–23]. Genetic selection for growth rate and lean muscle mass has altered physiological homeostasis, driving larger rates of muscle protein turnover that can precipitate muscle myopathies including woody breast[8]. In contrast, hindlimb muscles exhibit a mixed fibre-type composition and are functionally associated with locomotion and postural support, which results in more moderate and adaptive metabolic responses to selection for growth[22,24]. The liver plays a central homeostatic role in avian metabolism by coordinating systemic energy distribution, *de novo* lipogenesis, and nitrogen disposal via uric acid production[20,25], and is therefore expected to respond to increased metabolic demands imposed by rapid muscle growth primarily through adjustments in these core homeostatic functions.

Despite the fact that transcriptomic and proteomic studies have been conducted on fast-growing and slow-growing chickens, multi-omics approaches remain limited to the field of poultry research. The present study integrated transcriptomic data into an improved GSM chicken model to build context-specific models (CS-GSMs) describing tissue specificity for metabolic fluxes distribution. The metabolic predictions from CS-GSMs were then analysed and compared with results from transcriptomic and metabolomic profiling. Tissue-specific models were reconstructed based on the *i*ES1300[2] chicken model to assess growth-associated metabolic adaptations across breast muscle (BM), leg muscle (LM), and liver (LV).

We hypothesised that fast-growing chickens exhibit tissue-specific metabolic adaptations characterised by: (1) redistribution of metabolic flux in breast muscle away from classical oxidative pathways toward amino acid catabolism and one-carbon metabolism to support hypertrophic growth; (2) flexible metabolic adaptation in leg muscle to balance locomotion and growth demands through diversified pathway utilisation; (3) elevated TCA cycle activity alongside enhanced lipid metabolism and nitrogen disposal in liver, consistent with the established role of avian liver in coordinating systemic energy distribution, *de novo* lipogenesis, and nitrogen excretion[18,20,25]; and (4) that these tissue-specific adaptations would manifest as coordinated, directionally consistent signals across metabolic flux predictions, transcriptomic pathway enrichment, and metabolite concentration profiles, reflecting coherent transcriptional constraint on metabolic reprogramming.

## Results

### Phenotypic differences between FG and SG chickens

To conduct a comparative analysis of phenotypically divergent groups, we selected twelve fast-growing (FG) and twelve slow-growing (SG) $F_2$ offspring as the extremes of the 9-week body-weight distribution within each of the twelve maternal lineages (see Supplementary Table 1 for IDs and weights).

Across the panel of weight-related traits, FG consistently exceeded SG (Fig. 1). Biochemical serum parameters showed no statistically significant between-group differences after correction for multiple testing (Supplementary Table 1). For each trait, between-group contrasts were assessed by the Mann-Whitney U test with Benjamini-Hochberg FDR control ($p_{adj} < 0.05$);

effect sizes were summarized with Cliff's delta. Only weight-related traits passing FDR remained significant, confirming clear divergence in growth and body composition between groups and justifying downstream tissue-specific molecular analyses.

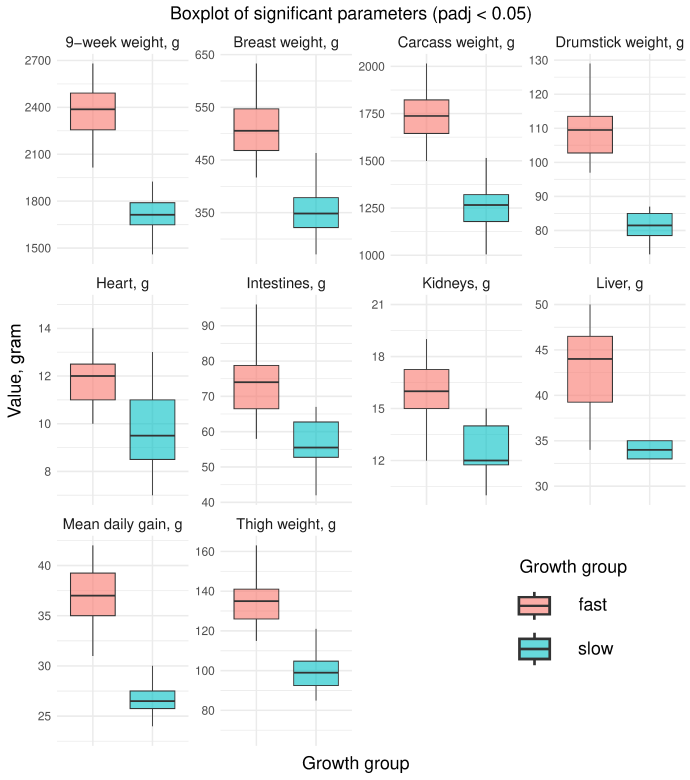



**Figure 1. Phenotypic traits differing between FG and SG.**
Boxplots show distributions (FG in pink, SG in cyan; $n = 12$ per group) for traits that remained significant after Benjamini-Hochberg correction: 9-week body weight, breast, carcass, drumstick, heart, intestines, kidneys, liver, mean daily gain, and thigh weights (all in grams).

## Metabolomic profiling reveals tissue-specific differences between FG and SG chickens

Metabolite profiles were measured across all three tissues, revealing that tissue identity is the primary driver of variance, with minimal separation between FG and SG groups within each tissue (see AMDB for detailed multivariate analysis).

We quantified 52 metabolites in breast muscle (BM), 57 in leg muscle (LM), and 74 in liver (LV) across all 24 animals (12 FG, 12 SG). In BM, pantothenate showed consistent elevation in FG chickens (HL/$\delta = 3.35$, $[0.69; 9.94]$, $p = 0.040$), while leucine (HL/$\delta = -3.55$, $[-5.56; -0.69]$, $p = 0.089$), valine (HL/$\delta = -2.15$, $[-6.71; 1.53]$, $p = 0.237$), glutamate (HL/$\delta = -1.69$, $[-5.11; 1.60]$, $p = 0.237$), and anserine (HL/$\delta = -2.67$, $[-7.22; 1.61]$, $p = 0.237$) exhibited lower abundance (Fig. 2A). Malonate showed a trend toward higher levels in FG (HL/$\delta = 2.76$, $[-1.76; 5.69]$, $p = 0.141$).

In LM, pantothenate was again elevated in FG (HL/$\delta = 4.08$, $[0.99; 8.06]$, $p = 0.030$), along with sarcosine (HL/$\delta = 3.25$, $[0.07; 7.64]$, $p = 0.053$), alanine (HL/$\delta = 3.42$, $[-1.30; 10.38]$, $p = 0.237$), 2-hydroxybutyrate (HL/$\delta = 2.72$, $[-0.91; 6.27]$, $p = 0.237$), and formate (HL/$\delta = 2.49$, $[-1.16; 5.39]$, $p = 0.157$) (Fig. 2B). Pantothenate was the only metabolite consistently elevated across both muscle types.

The liver showed distinct metabolic patterns. Glutamate (HL/$\delta = 3.37$, $[-0.65; 6.88]$, $p = 0.157$) and glucose (HL/$\delta = 2.70$, $[-1.69; 4.72]$, $p = 0.157$) exhibited elevation in FG chickens, while uracyl showed lower abundance in FG (HL/$\delta = -2.50$, $[-5.64; 1.13]$, $p = 0.141$) (Fig. 2C).

The modest metabolite changes, consistent with homeostatic buffering, prompted transcriptomic analysis to capture upstream regulatory responses driving the observed phenotypic differences. For more detailed information on the results of the experiments, please refer to the Data Availability Statement.

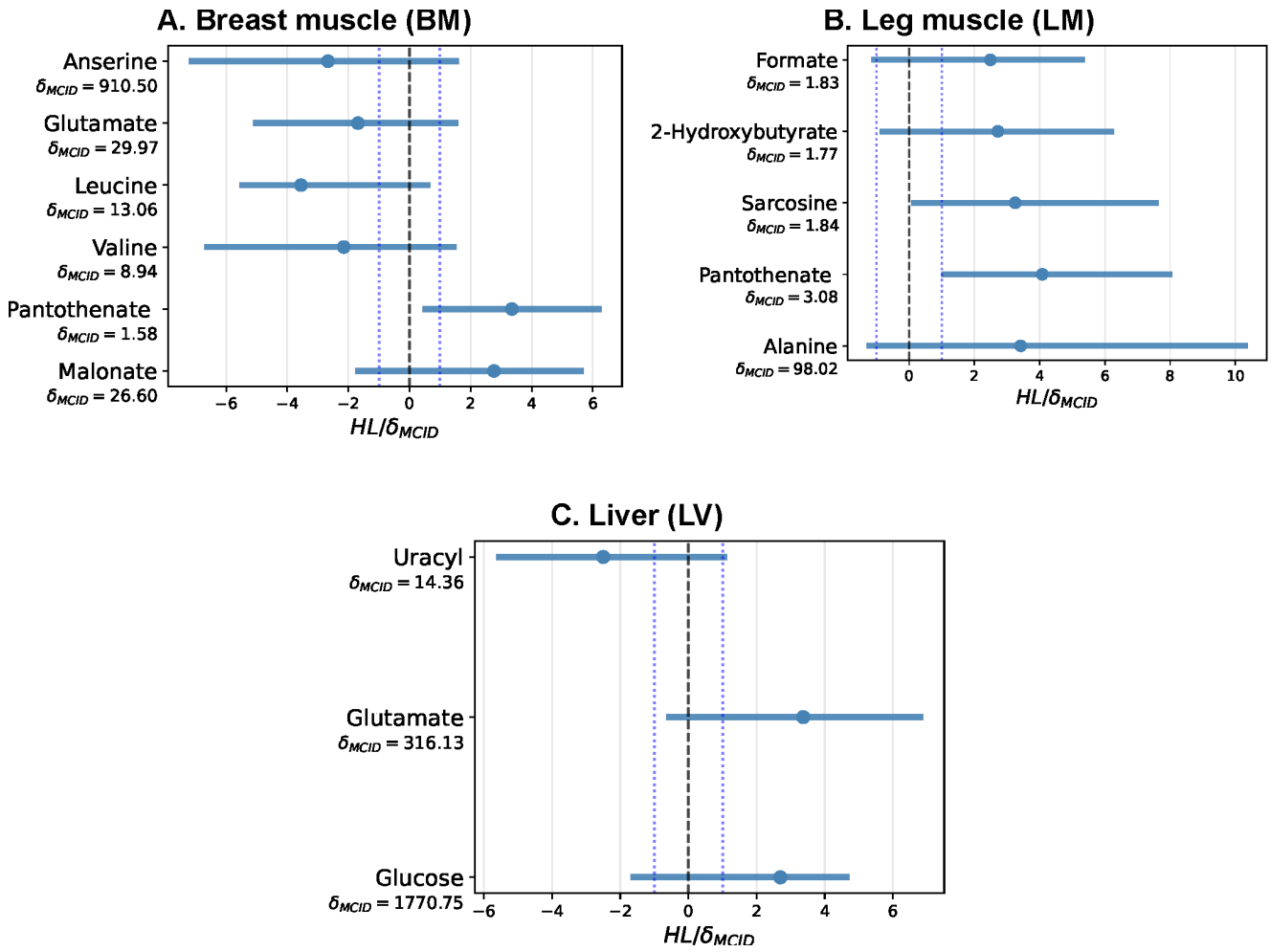



**Figure 2. Forest plots of Hodges-Lehmann effects relative to metabolite-specific Cohen's "small effect"($\delta$).** Within-tissue differences in metabolite concentrations between fast- (FG) and slow-growing (SG) groups. Panels: (A) Breast muscle (BM); (B) Leg muscle (LM); (C) Liver (LV). For each metabolite, points denote the Hodges-Lehmann estimator of the FG-SG difference ($\mathrm{HL} = \mathrm{median}_{i,j}(x_i - y_j)$); horizontal bars represent 95% bootstrap confidence intervals. Values are expressed as $\mathrm{HL}/\delta_i$; vertical dotted lines indicate $\pm 1$. Positive HL indicates higher concentrations in FG; negative HL indicates higher concentrations in SG.

### Transcriptomic profiling of liver, leg, and breast tissues from fast- and slow-grown chickens

Differential expression analysis identified 12,314 genes in breast muscle (BM), 16,176 in leg muscle (LM), and 17,423 in liver (LV) passing DESeq2's independent filtering and included in downstream analyses. Of these, 443, 1,279, and 1,587 genes were significantly differentially expressed (FDR $< 0.05$) in BM, LM, and LV, respectively. Pre-ranked GSEA on the complete ranked gene lists revealed significant GO Biological Process enrichment across all three tissues (FDR $< 0.05$; Fig. 3; Supplementary Table 2).

Cross-tissue comparison revealed both shared and tissue-specific enrichment patterns (Fig. 3). Terms enriched in at least two tissues included hypoxia and oxygen-level response programs (upregulated in BM and LM), Wnt and receptor tyrosine kinase signaling pathways (upregulated in BM and LM), mitotic cell cycle processes (downregulated across all three tissues), and cellular component assembly, biogenesis, and organelle organization (downregulated in LM and LV). Several pathways exhibited tissue-specific enrichment (Supplementary Table 2): BM showed upregulation of immune system processes and developmental programs alongside downregulation of small molecule metabolism; LM displayed enrichment in amide and protein metabolic processes; while LV showed specific enrichment in protein-containing complex organization. These transcriptional shifts — encompassing hypoxia-response signatures, coordinated suppression of cell division, and tissue-specific metabolic reprogramming — prompted constraint-based metabolic flux modeling to resolve how gene expression changes translate into pathway-level redistribution of metabolic activity.

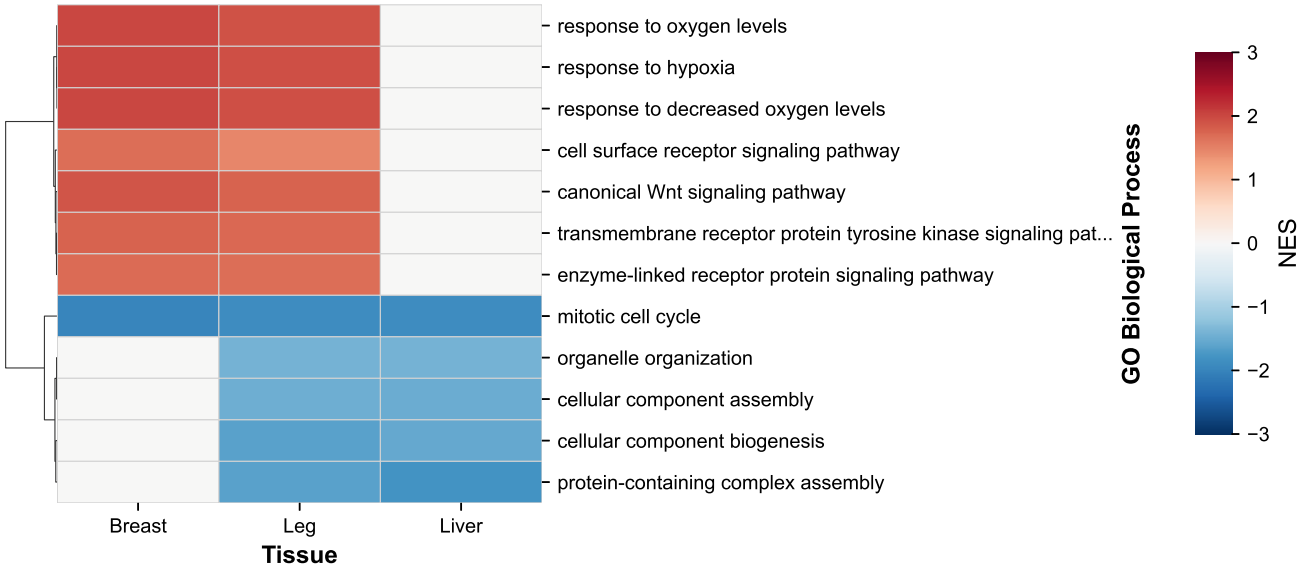



**Figure 3. Normalized enrichment scores (NES) from pre-ranked GSEA of GO Biological Process terms enriched in at least two tissues** (FDR $< 0.05$)**.** Each row represents a GO:BP term; columns correspond to breast muscle (BM), leg muscle (LM), and liver (LV). Colour encodes NES: red indicates upregulation and blue indicates downregulation in fast-growing relative to slow-growing birds. Empty cells indicate terms that did not reach significance in the respective tissue (FDR $< 0.05$). Rows are ordered by hierarchical clustering of NES values. Complete tissue-specific enrichment results are provided in Supplementary Table 2.

## Model Quality Enhancement

To improve the structural reliability and biophysical consistency of the *i*ES1300 genome-scale metabolic model, a series of targeted refinements were performed, resulting in an updated reconstruction hereafter referred to as *i*ES1470. These refinements addressed mass and charge imbalances, annotation incompleteness, and network connectivity issues that could compromise flux-based analyses.

As part of model curation, a cytosolic spermine demand reaction was added to the single demand reaction (dGTP, mitochondrial) already present in *i*ES1300, serving as a terminal sink for polyamine biosynthesis, which is well-documented in avian tissues[26]. Three intracellular source/sink reactions lacking physiological justification (`SK_Tyr_ggn_c`, `SK_btn(c)`, `SK_pmtcoa_c`) were removed, along with three additional reactions identified during manual curation (Supplementary Table 2). Chemical formulas were assigned to all 2,570 metabolites using curated biochemical databases, including PubChem[27], BiGG[28], MetaNetX[29], and ChEBI[30]. In parallel, 44 reactions were corrected or redefined based on reference reactions from Recon3D and cross-validated using BiGG[28], SEED/RAST[31], BioCyc/Pathway Tools[32], and MetaNetX[29] (Supplementary Table 2, sheet 1).

MACAW-based diagnostics revealed structural inconsistencies related to erroneous reaction reversibility and the presence of thermodynamically infeasible loops. Transport reactions introduced during refinement were explicitly evaluated for loop formation, and reactions identified as participating in closed cycles were removed. These corrections improved the energetic feasibility of the network; the marginal increase in loop-forming reactions from 232 to 234 reflects residual interactions introduced by HumanGEM-derived transport reactions that were not fully resolved during curation.

Mass and charge balance inconsistencies were resolved for 866 of 916 previously unbalanced reactions, resulting in a substantial improvement in overall stoichiometric quality. Following refinement, the proportion of mass-imbalanced reactions decreased from 100.0% in *i*ES1300 to 1.43% in *i*ES1470, while the proportion of charge-imbalanced reactions decreased from 2.77% to 1.27% (Table 1). The 100% mass imbalance in *i*ES1300 reflects the complete absence of metabolite chemical formulas in the original reconstruction, which precluded Memote from evaluating mass balance for any reaction. A complete list of modifications is provided in Supporting Information (Supplementary Table 3, sheet 1).

A substantial fraction of dead-end metabolites in *i*ES1300 was associated with compartment-specific species in subcellular organelles (e.g., mitochondria, endoplasmic reticulum, peroxisomes, Golgi apparatus, nucleus) that lacked intracellular transport

reactions connecting them to the cytosol. These are distinct from exchange reactions, which define metabolite fluxes across the extracellular boundary of the model. To address this limitation, intracellular transport reactions linking organellar compartments to the cytosol were systematically transferred from the HumanGEM reconstruction. In total, 354 transport reactions were extracted, standardized to a unified naming convention, and incorporated into the model. Following MACAW-based loop detection, reactions participating in thermodynamically infeasible cycles were removed, yielding a final curated set of 246 HumanGEM-derived intracellular transport reactions (Supplementary Table 3, sheet 2). All transferred reactions were prefixed with `HUMANGEM_` to preserve traceability and denote reactions requiring additional validation.

The integration of HumanGEM-derived transport reactions improved network connectivity, reducing dead-end metabolites from 513 to 434 (19.97% to 16.89%) and orphan metabolites from 403 to 337 (15.69% to 13.11%) according to Memote structural analysis (Table 1). However, the overall effect on network connectivity was modest: a substantial fraction of dead-end metabolites persisted because they require additional intracellular reactions rather than transport connections. These residual connectivity issues represent priorities for future curation.

As a result of these refinements, the final curated *i*ES1470 model comprised 1,470 genes, 2,570 metabolites, and 2,698 reactions.

Overall improvements were assessed using the Memote test suite (v0.16.1)[33]. Comparison of *i*ES1300 and *i*ES1470 revealed a substantial increase in model quality, with the total Memote score improving from 18.06% to 37.92%. Improvements were observed across multiple quality metrics, including stoichiometric consistency section score (38.15% to 52.91%), annotation coverage, and network connectivity (Table 1). Both models failed the binary stoichiometric consistency test[34], indicating the presence of unconserved metabolites; the number of unconserved metabolites reported by Memote increased from 589 to 745, partly due to the expansion of the metabolite pool and the introduction of transport reactions connecting previously isolated compartments. Gene annotation coverage remained at 0% in both models, as chicken gene identifiers were not mapped to standard cross-reference databases supported by Memote; this represents a priority for future annotation work.

**Table 1.** Comparison of model quality metrics for *i*ES1300 and *i*ES1470 genome-scale metabolic models assessed using Memote v0.16.1.

| Metric | *i*ES1300 | *i*ES1470 |
|---|---|---|
| Charge-imbalanced reactions (%) | 2.77 | 1.27 |
| Mass-imbalanced reactions (%) | 100.00 | 1.43 |
| Dead-end metabolites (%) | 19.97 | 16.89 |
| Orphan metabolites (%) | 15.69 | 13.11 |
| Consistency section score (%)[a] | 38.15 | 52.91 |
| Reaction annotation coverage (%) | 43.53 | 65.92 |
| Metabolite annotation coverage (%) | 0.00 | 65.21 |
| SBO term coverage (%) | 0.00 | 18.73 |
| Total Memote score (%) | 18.06 | 37.92 |

[a]The consistency section score is the aggregate Memote score for the consistency test category, comprising stoichiometric, mass balance, charge balance, and network connectivity sub-tests. Both models additionally failed the binary stoichiometric consistency test (pass/fail) based on the algorithm of[34].

Collectively, these refinements resulted in a structurally robust and well-annotated metabolic reconstruction, providing a reliable foundation for subsequent context-specific model reconstruction and comparative flux analyses.

### Differential pathway analysis from RIPTiDe-derived fluxomes

To verify the effect of observed transcriptional patterns on the metabolic flux redistribution, we integrated tissue-specific expression profiles into refined constraint-based model. We summarized differential reaction fluxes (DRFs) by metabolic subsystem using reaction-level Differential Pathway Flux Analysis (r-DPFA) and quantified per-metabolite throughput within subsystems using metabolite-centered Differential Pathway Flux Analysis (mc-DPFA; $log_2$ fold-change of per-metabolite total flux of pathways, FG/SG). This two-level approach allows us to first identify large-scale pathway shifts and then pinpoint the specific metabolites driving them.

The r-DPFA provides a high-level overview of pathway activity shifts by summarizing the composition and directionality of DRFs within each subsystem (Fig. 4; Supplementary Table 4). In contrast, mc-DPFA resolves how these pathway-level alterations are distributed across individual metabolites, thereby revealing localized reorganization of metabolic throughput that may not be apparent from reaction counts alone (Fig. 5; Supplementary Table 5). Together, these complementary approaches enable both pathway-scale quantification and metabolite-specific mechanistic insights into flux redistribution.

In breast muscle (BM), pathway-level remodeling was comparatively modest but directionally coherent (Figs. 4A, 5A).

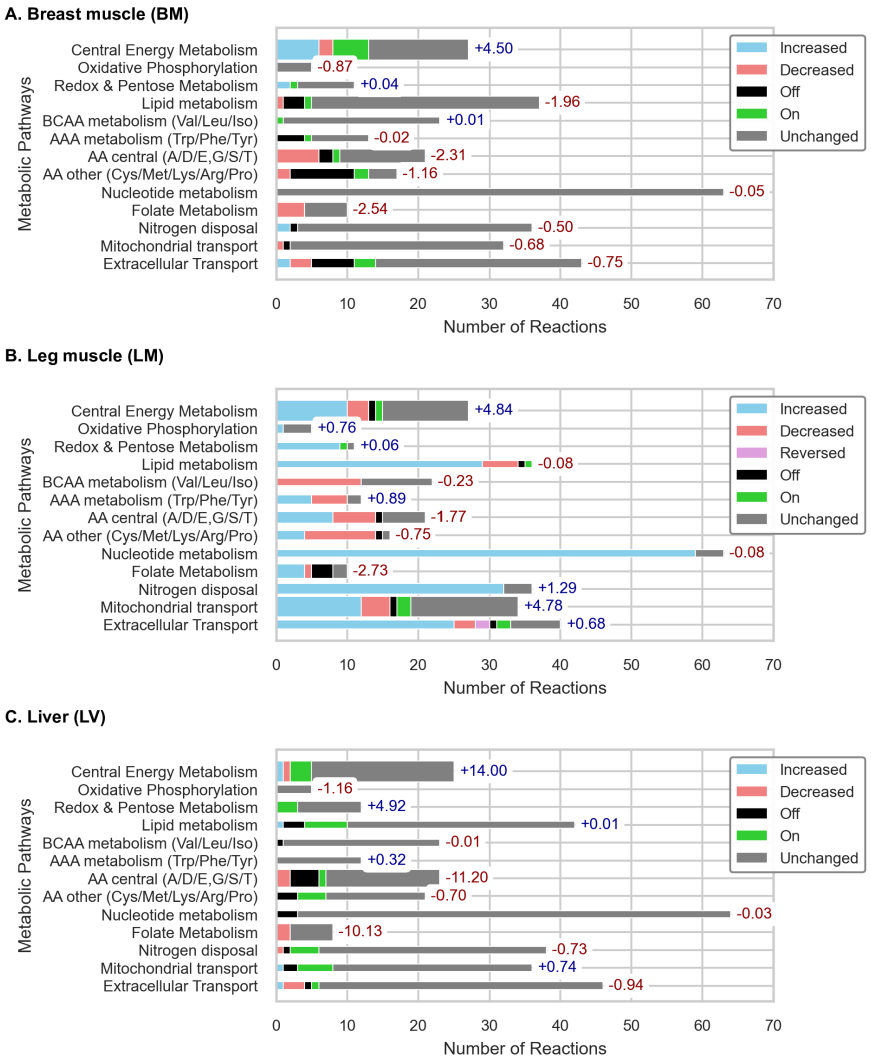



**Figure 4. Reaction-level Differential Pathway Flux Analysis (r-DPFA): DRF composition by subsystem (FG vs. SG).** Stacked bars show DRF counts per subsystem for (A) breast muscle, (B) leg muscle, and (C) liver. Bar thickness encodes normalised $\Delta_P$; numeric annotations show raw $\Delta_P$ values (positive = net flux increase in FG).

Central energy metabolism showed the largest net flux increase ($\Delta_P = +4.50$), driven by elevated flux through TCA cycle reactions (AKGDm, FUMm, SUCOASm, PCm, ME2m) and five newly activated mitochondrial entry steps, while oxidative phosphorylation declined modestly ($-0.87$) with all five reactions Unchanged in category — consistent with an enhanced glycolytic bias characteristic of fast-growing breast muscle. Lipid metabolism decreased ($-1.96$) via inactivation of mitochondrial $\beta$-oxidation reactions (ECOAH1m, HACD1m), accompanied by a marked reduction in DHAP turnover ($\log_2 \mathrm{FC} \approx -2$ to $-8$ across subsystems), limiting glycerol-3-phosphate availability for glycerophospholipid synthesis.

Amino acid subsystems were broadly suppressed, yet mc-DPFA revealed selective redistribution within this overall decline. AA central ($\Delta_P = -2.31$) and AA other ($-1.16$) showed reduced flux through serine biosynthesis (PGCD, PSERT, GHMT2rm), glycine cleavage, and lysine catabolism (SACCD3m), with L-glutamate and $\alpha$-KG qualitatively abolished in nitrogen disposal ($\approx -6$, via GLUDxm inactivation) and moderately reduced in BCAA and AA central ($\approx -1$ to $-3$). Against this backdrop, pyruvate and L-alanine were qualitatively activated in AA central and AA other ($\approx +6$, via ALATA_L), while alanine extracellular transport declined ($\approx -2$) — indicating net intracellular alanine synthesis serving as a nitrogen buffer under suppressed nitrogen disposal. Lysine showed the inverse pattern: catabolism blocked ($\approx -6$) but exogenous import maintained (LYSt5r: FG $\approx 4.60 \times 10^{-2}$, SG $\approx 3.53 \times 10^{-2}$ mmol gDW$^{-1}$ h$^{-1}$), suggesting preferential uptake for biomass rather than recycling. Folate metabolism decreased ($\Delta_P = -2.54$, four reactions Decreased), yet nucleotide metabolism remained

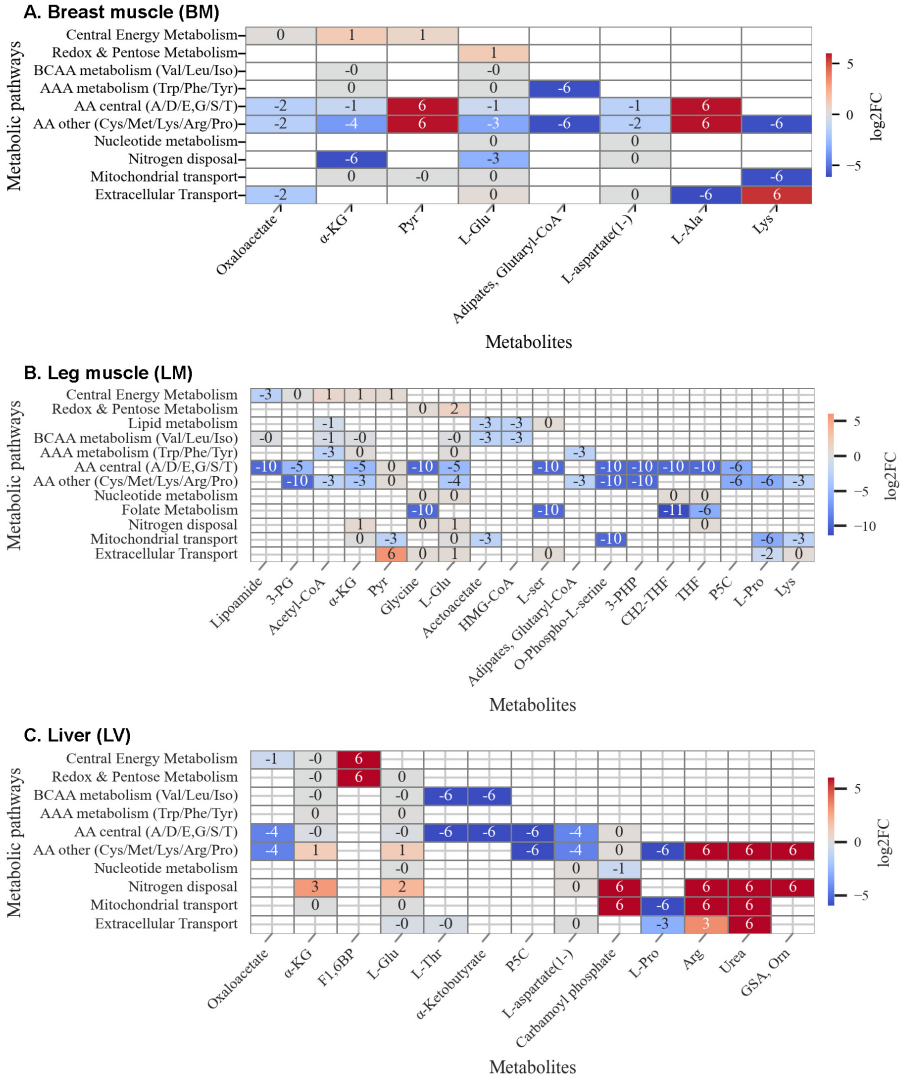



**Figure 5. Metabolite-centred Differential Pathway Flux Analysis (mc-DPFA): per-metabolite pathway flux $\log_2$FC (FG/SG).** Heatmaps show $\log_2(\mathrm{FG}/\mathrm{SG})$ of summed metabolite-associated fluxes for (A) breast muscle, (B) leg muscle, and (C) liver. Only metabolites with $|\log_2 \mathrm{FC}| > 1.0$ in at least two pathways are shown; $\pm 6$ denotes qualitative on/off states.

essentially unchanged ($-0.05$, all 63 reactions Unchanged), with glycine redistributed toward pentose phosphate flux ($\approx +1$) rather than one-carbon transfer.

In the leg muscle (LM), r-DPFA revealed a more balanced metabolic remodelling compared to the breast muscle. Central energy metabolism showed the largest total flux shift ($+4.84$ mmol gDW$^{-1}$ h$^{-1}$), driven by marked acceleration of TCA cycle reactions (*ACONTm*, *CSm*, *ICDHxm*; ratio $\sim$2.64) and pyruvate dehydrogenase (*PDHm*; ratio 3.59). Oxidative phosphorylation, however, increased only modestly ($+0.76$), with respiratory chain reactions remaining near unity, suggesting a shift in energy substrate utilisation without proportional expansion of mitochondrial ATP synthesis—in contrast to the glycolytic bias observed in the breast muscle. Mitochondrial transport showed a comparable flux shift ($+4.78$ mmol gDW$^{-1}$ h$^{-1}$), corroborating active Krebs cycle engagement.

Amino acid catabolism was broadly suppressed: the central amino acid subsystem declined ($-1.77$ mmol gDW$^{-1}$ h$^{-1}$) due to inactivation of the glycine cleavage system and serine synthesis branch, while other amino acid pathways also decreased ($-0.75$ mmol gDW$^{-1}$ h$^{-1}$). Unlike the breast muscle, extracellular amino acid import remained active ($+0.68$ mmol gDW$^{-1}$ h$^{-1}$); 25 reactions increased). Within AAA metabolism, flux redistribution toward tryptophan oxidation (*TRPO2*, *KYN3OX*, *FKYNH*) was accompanied by stable phenylalanine transamination (*PHETA1*/*PHETA1m*; ratio $\sim 1.05$). Glutamate dehydrogenase (*GLUDxm*; ratio 1.85) accelerated across subsystems, supporting enhanced amino group mobilisation; accordingly, nitrogen

disposal was the only positively shifted amino acid subsystem (+1.29 mmol $gDW^{-1}$ $h^{-1}$), driven by the purine nucleotide cycle and urea-cycle intermediates.

Nucleotide metabolism showed a paradoxical pattern: 59 reactions were classified as increased, yet the net flux shift was marginally negative (−0.08 mmol $gDW^{-1}$ $h^{-1}$), as high-flux reactions (*ADK1*, *ATPM*) remained largely unchanged. Folate metabolism declined substantially (−2.73 mmol $gDW^{-1}$ $h^{-1}$), with THF turnover strongly decreased ($\log_2 FC = -5.82$) following inactivation of the glycine cleavage system. The four folate reactions classified as increased (*AICART*, *FTHFL*, *GARFT*, *r0226*) are components of de novo purine synthesis and reflect demand imposed by the accelerated nucleotide biosynthesis rather than independent folate cycle activation.

In liver (LV), metabolic response was characterised predominantly by qualitative on/off transitions rather than graded flux changes, with relatively few reactions classified as Increased or Decreased (Fig. 4C). This pattern was particularly evident in key subsystems: nitrogen disposal gained four reactions (ARGNm, ORNTArm, r0034, r0074) while losing one (PUNP3), and lipid metabolism activated six new routes while simultaneously losing three, with net flux shifts remaining modest despite substantial qualitative reorganisation. This suggests a discrete switch in hepatic metabolic state rather than continuous scaling of pathway activity.

Central energy metabolism showed the largest net flux increase ($\Delta_P = +13.99$), driven by activation of glycolysis (PFK, PGI) and pyruvate dehydrogenase (PDHm), with acetyl-CoA turnover increasing substantially in both the citric acid cycle ($\log_2 FC \approx +1.40$) and glycolysis ($\approx +1.85$). Oxidative phosphorylation decreased modestly ($\Delta_P = -1.16$), with all five OXPHOS reactions showing uniformly reduced flux, indicating attenuation rather than suppression of mitochondrial ATP synthesis. Redox & pentose metabolism increased ($\Delta_P = +4.92$) through activation of three reactions (FBA, G6PDH1rer, PGLer), consistent with elevated NADPH and ribose-5-phosphate demand.

Folate metabolism decreased markedly ($\Delta_P = -10.13$), with complete loss of MTHFD2m and downregulation of two further reactions. Concordantly, CH2-THF, THF, glycine, serine, and O-phosphoserine all showed $\log_2 FC \approx -9.8$ within folate and serine/glycine pathways, reflecting shutdown of the mitochondrial glycine cleavage system in FG liver.

Extracellular transport showed mixed directionality: arginine–lysine exchange increased markedly and urea export (UREAt) was newly activated, consistent with enhanced ureagenesis, while uptake of glutamate, proline, and ammonium was reduced, reflecting decreased reliance on exogenous nitrogen as internal amino acid catabolism intensified. L-proline and P5C were lost from both mitochondrial transport and arginine/proline pathways ($\log_2 FC = -6$), indicating suppression of the proline–ornithine axis. BCAA metabolism was near-neutral overall ($\Delta_P = -0.01$), with HMG-CoA and acetoacetate turnover reduced in ketone body pathways ($\log_2 FC \approx -2.5$) while acetyl-CoA entry into the TCA cycle increased.

Together, r-DPFA and mc-DPFA reveal tissue-partitioned metabolic strategies in rapid growth. Breast muscle maintained stable pathway throughput with selective amino acid and one-carbon reorganisation; leg muscle exhibited broadly distributed flux increases with pronounced lipid and ketone body engagement; liver displayed the most extensive flux redistribution, characterised by qualitative on/off switching of entire pathway blocks alongside enhanced central carbon metabolism and reduced oxidative phosphorylation. Across all tissues, mc-DPFA identified metabolite-level redistributions not apparent from pathway-level metrics, particularly within subsystems showing near-zero net flux change.

## Concordance of context-specific flux predictions with transcriptomic changes

To assess the agreement between transcriptomic information and predicted metabolic fluxes, we quantified concordance between transcript-derived reaction effects and median absolute reaction fluxes using the RIPTiDe concordance framework (see Methods). Across all tissues and growth conditions, Spearman rank correlations were positive and statistically significant, albeit modest in magnitude (Table 2). Such correlation ranges are typical for constraint-based metabolic models and reflect the fact that transcriptional regulation captures only a subset of the regulatory mechanisms governing steady-state flux distributions.

Reaction-level transcript–flux concordance was examined using TFCA by comparing FG/SG flux ratios with transcript-derived reaction effects aggregated via GPR rules (Fig. 6; Supplementary Table 6). Results are discussed below for each tissue separately, focusing on reactions that satisfied both transcript-level and flux-level significance thresholds.

In breast muscle (Fig. 6A), concordant activation was observed for alanine aminotransferase (ALATA_L; GPT2, transcript $\log_2 FC \approx +2.37$, $q < 0.001$), pyruvate dehydrogenase (PDHm; DLAT, transcript $\log_2 FC \approx +2.34$, $q = 0.010$), and citrate synthase (CSm; CS, transcript $\log_2 FC \approx +1.01$, $q = 0.029$), all showing qualitative flux activation ($\log_2$ ratio $= +3$). Concordant suppression was observed for mitochondrial $\beta$-oxidation (ECOAH1m; transcript $\log_2 FC \approx -0.52$, flux $\log_2$ ratio $= -3$, $q = 0.878$). The most prominent discordant reaction was glutamate dehydrogenase (GLUDxm; GLUD2), which exhibited strong transcript-level upregulation ($\log_2 FC \approx +2.47$, $q < 0.001$) accompanied by qualitative flux suppression ($\log_2$ ratio $= -3$), consistent with post-transcriptional or allosteric attenuation of glutamate oxidation despite elevated enzyme expression. Additional discordant reactions included mitochondrial lysine transport (LYStm; $\log_2$ ratio $= -3$ versus transcript $\log_2 FC \approx +0.88$, $q = 0.074$) and tryptophan catabolism (r0541; GCDH, transcript $\log_2 FC \approx +0.55$, flux $\log_2$ ratio $= -3$, $q = 0.201$). Phosphoserine aminotransferase (PSERT; PSAT1, $q = 0.010$) showed moderate transcript upregulation

**Table 2. Context-specific growth and concordance with transcriptomics.**

| Model | $\mu_{CS}$ | $\Delta\%$ | $\rho$ ($p$) |
|---|---|---|---|
| fast-breast CS-GSM | 0.0342 | 0.0% | 0.298 ($< 0.001$) |
| slow-breast CS-GSM | 0.0342 | 0.0% | 0.326 ($< 0.001$) |
| fast-leg CS-GSM | 0.024 | −29.82% | 0.31 ($< 0.001$) |
| slow-leg CS-GSM | 0.0172 | −49.71% | 0.285 ($< 0.001$) |
| fast-liver CS-GSM | 0.009 | −73.68% | 0.2 ($< 0.001$) |
| slow-liver CS-GSM | 0.008 | −76.32% | 0.17 ($= 0.001$) |

Baseline growth rate of the generic GSM is $\mu_{GSM} = 0.0342$ mmol gDW$^{-1}$ h$^{-1}$). $\mu_{CS}$ denotes the growth rate of the context-specific GSM (CS-GSM); $\Delta\% = 100(\mu_{CS}/\mu_{GSM} - 1)$. Correlations ($\rho$) are Spearman's rank correlation coefficients between transcript-derived reaction effects and predicted flux ratios; $p$ denotes the associated significance level.

($\log_2$ FC $\approx +0.84$) with attenuated flux response ($\log_2$ ratio $\approx -0.74$), indicating network-level buffering of serine biosynthesis despite transcriptional induction.

In leg muscle (Fig. 6B), concordant reactions spanned a broader dynamic range. Pyruvate dehydrogenase (PDHm; DLAT) showed the strongest concordant activation (transcript $\log_2$ FC $\approx +3.18$, $q < 0.001$; flux $\log_2$ ratio $\approx +1.84$), followed by citrate synthase (CSm; transcript $\log_2$ FC $\approx +1.18$, $q = 0.011$; flux $\log_2$ ratio $\approx +1.40$) and glutamate dehydrogenase (GLUDxm; transcript $\log_2$ FC $\approx +1.05$, $q = 0.009$; flux $\log_2$ ratio $\approx +0.89$). Notably, GLUDxm was concordant in leg muscle but discordant in breast muscle, indicating tissue-specific decoupling of glutamate oxidation from transcriptional regulation. Mitochondrial CoA transport (COAtim; SLC25A16, transcript $\log_2$ FC $\approx +1.16$, $q = 0.027$) and glutathione-related reactions (r0130; GGT2/GGT2P, transcript $\log_2$ FC $\approx +0.89$) showed qualitative flux activation. Concordant suppression of $\beta$-oxidation (ECOAH1m; transcript $\log_2$ FC $\approx -0.59$, $q = 0.188$; flux $\log_2$ ratio $\approx -2.47$) was consistent with the pattern observed in breast muscle. The most striking discordances in leg muscle involved the serine–glycine–one-carbon axis: serine hydroxymethyltransferase (GHMT2rm; SHMT1, transcript $\log_2$ FC $\approx +1.77$, $q < 0.001$) and phosphoserine aminotransferase (PSERT; PSAT1, transcript $\log_2$ FC $\approx +0.98$, $q < 0.001$) both exhibited strong transcript upregulation accompanied by qualitative flux suppression ($\log_2$ ratio $\approx -6.64$), indicating network-level override of transcriptional induction within this pathway. Similarly, ketone body synthesis reactions (HMGCOASim and HMGLm; transcript $\log_2$ FC $\approx +0.98$–$1.42$, $q = 0.021$–$0.027$) showed concordant flux suppression ($\log_2$ ratio $\approx -2.47$), suggesting substrate-level or thermodynamic constraints limiting ketogenic flux despite transcriptional activation of the relevant enzymes.

In liver (Fig. 6C), the predominance of on/off flux transitions identified by r-DPFA was reflected at the reaction level in TFCA. Pyruvate dehydrogenase (PDHm; DLAT, transcript $\log_2$ FC $\approx +2.88$, $q < 0.001$), urea export (UREAt; SLC5A1, transcript $\log_2$ FC $\approx +2.32$, $q = 0.008$), carbamoyl phosphate synthetase (r0034; CPS1, transcript $\log_2$ FC $\approx +1.13$, $q = 0.030$), and arginase (ARGNm; ARG2) all exhibited concordant qualitative activation ($\log_2$ ratio $= +3$), consistent with enhanced ureagenesis in FG liver. The most pronounced flux-dominant response was observed for hexokinase (HEX1; $\log_2$ flux ratio $\approx +9.76$, transcript $\log_2$ FC $\approx +0.10$), indicating strong network-driven amplification of glycolytic entry independent of transcriptional regulation. Carbonic anhydrase (r1418m; CA5A) showed concordant suppression (transcript $\log_2$ FC $\approx -0.57$, flux $\log_2$ ratio $\approx -0.94$, $q = 0.203$). All four OXPHOS reactions with available flux data (ATPS4m, CYOOm3, CYOR_u10m, NADH2_u10m) exhibited concordant decreases in both transcript-derived effects and predicted fluxes, corroborating the pathway-level OXPHOS attenuation identified by r-DPFA. The sole discordant significant reaction was 2-hydroxybutyrate transport (2HBt2; SLC16A1, transcript $\log_2$ FC $\approx +0.52$, flux $\log_2$ ratio $= -3$, $q = 0.413$), suggesting post-transcriptional regulation or metabolite-level suppression of this transport step.

Across all tissues, no statistically significant reactions exhibited opposing transcript-derived and flux-based directionality, indicating that transcriptional regulation provides coherent directional constraints on metabolic flux redistribution. Discordant reactions were systematically interpretable as instances of post-transcriptional attenuation, allosteric control, or network topology-driven flux amplification, rather than conflicting regulatory signals.

## Discussion

Our multi-omics analysis of $F_2$ cross individuals revealed tissue-specific metabolic adaptations underlying divergent growth rates in chickens. Despite pronounced phenotypic differences between fast-growing and slow-growing birds, metabolite concentrations exhibited only modest between-group variation, consistent with homeostatic buffering mechanisms[35]. In contrast, transcriptional profiling captured broader patterns of differential gene regulation. Flux-based modeling bridged these layers by resolving how transcriptional changes translate into pathway-level redistribution of metabolic throughput, thereby

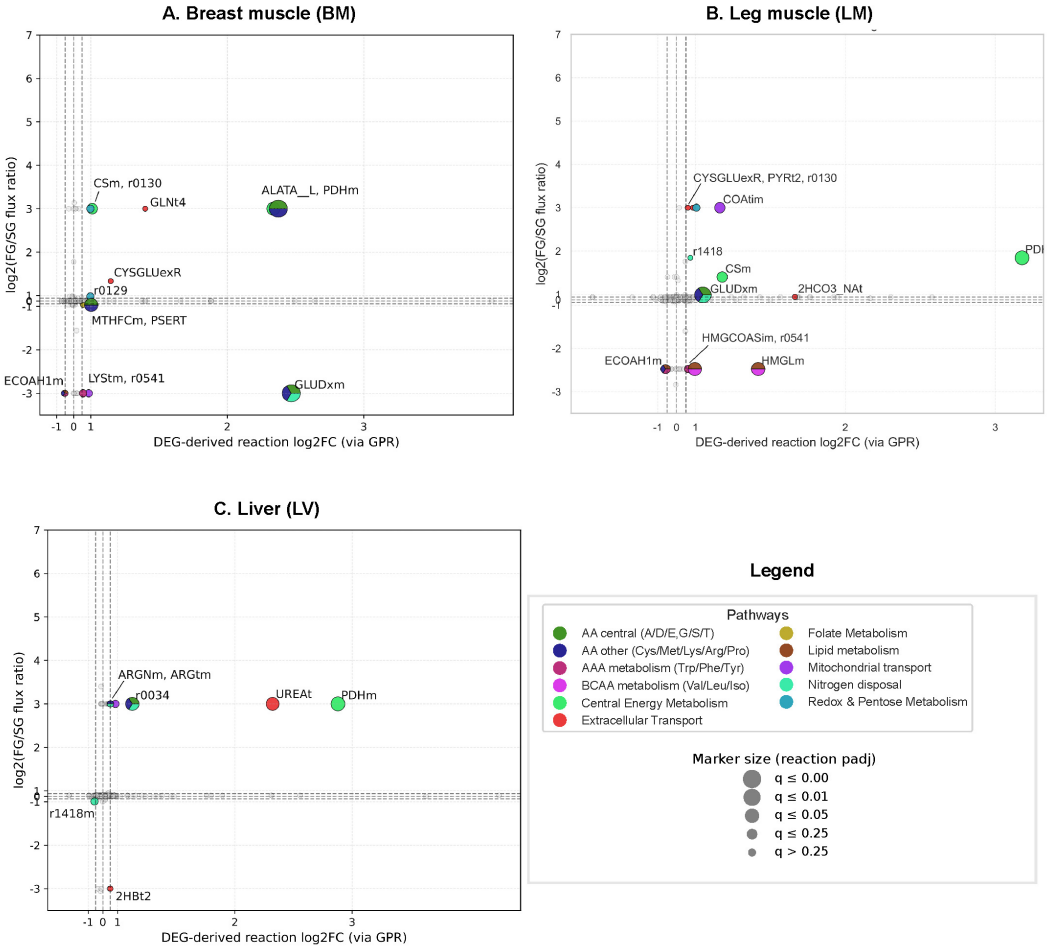



**Figure 6. Reaction-level concordance between transcript-derived reaction effects and predicted flux ratios (FG/SG).** Scatter plots compare transcript-derived reaction effects (x-axis: $L_r$, $\log_2$FC via GPR rules) with predicted flux ratios (y-axis: $F_r$, $\log_2$ FG/SG; reactions active in only one group mapped to $\pm 3$) for (A) breast muscle, (B) leg muscle, and (C) liver. Dashed lines indicate magnitude thresholds ($|L_r| \geq 0.50$, $|F_r| \geq 0.50$), corresponding to transcript-level and flux-level significance cutoffs, respectively. Points that satisfied both thresholds are colored by metabolic pathway; marker size reflects reaction-level adjusted $p$-value. Reactions that reversed net direction are excluded from plots but included in quantitative summaries.

linking regulatory signals to buffered metabolite end states. Integration of these data layers through constraint-based flux modeling enabled identification of coordinated metabolic strategies that are not apparent from single-omics analyses alone.

Breast muscle exhibited depletion of several amino acids despite elevated anabolic demand, with carbon flux preferentially redirected toward amino acid catabolism and one-carbon metabolism rather than classical oxidative pathways. OXPHOS and mitochondrial transport fluxes declined modestly ($\Delta_P = -0.87$ and $-0.68$, respectively), yet the broadest metabolite-level flux redistribution occurred in AA central, AAA metabolism, and folate pathways, a pattern consistent with early-stage metabolic stress preceding the mitochondrial dysfunction and impaired OXPHOS complex activity documented in woody-breast-affected broilers[16,17]. Transcriptomic profiling of breast muscle further revealed tissue-specific upregulation of signaling and developmental programs, consistent with muscle fiber enlargement driven by satellite cell fusion rather than proliferation[36,37]. Leg muscle displayed metabolite accumulation and increased pathway turnover, with pronounced lipid and ketone body engagement; this flexibility aligns with the distinct mitochondrial contents and respiratory capacities reported across chicken skeletal muscle fibre types[19]. In the liver, central energy metabolism and TCA cycle activity were markedly elevated while OXPHOS flux and mitochondrial transport were reduced. This finding indicates that hepatic energy provision relied on enhanced glycolytic throughput and amino acid catabolism rather than oxidative phosphorylation itself[38,39], consistent with reports of divergent metabolism between meat-type and layer-type chicken lines[18,20]. Glucose accumulation alongside reduced nucleotide and nitrogen disposal pathway activity further suggested metabolic stress under rapid growth conditions. Metabolite-level changes, though modest and largely below conventional significance thresholds, were directionally consistent with

these flux predictions: lower leucine, valine, and glutamate in breast muscle corroborate amino acid catabolism; alanine and 2-hydroxybutyrate accumulation in leg muscle align with gluconeogenic export and enhanced fatty acid oxidation; and elevated hepatic glucose and glutamate alongside reduced uracil support increased central carbon catabolism and attenuated nucleotide metabolism. Pantothenate elevation across both muscle tissues may reflect increased CoA demand under conditions of enhanced lipid and energy metabolism. Cross-tissue transcriptomic comparison further revealed shared enrichment of hypoxia-response programs and canonical Wnt signaling across both muscle tissues, alongside coordinated downregulation of mitotic cell cycle processes across all three tissues. The co-occurrence of active Wnt signaling — a key driver of satellite cell activation and myogenic differentiation — with suppressed cell cycle activity is consistent with a shift from proliferative to hypertrophic muscle growth[36,37], while the shared hypoxia transcriptional signature aligns with elevated oxygen consumption and limited oxygen delivery documented in fast-growing broilers[10,11,14]. Across all three omics layers, these patterns converged on a coherent picture of tissue-partitioned metabolic reprogramming under rapid growth conditions.

These tissue-specific patterns align well with established broiler physiology. Fast-growing chickens are predisposed to panting, heat sensitivity, hypoxia, and ascites[10,11,14], conditions commonly attributed to elevated metabolic rates combined with limited thermoregulatory capacity. Our results provide molecular support for these phenotypes, revealing enhanced mitochondrial transport and oxidative phosphorylation in skeletal muscle[40,41], elevated central carbon metabolism and amino acid catabolism in liver with reduced oxidative phosphorylation and mitochondrial transport capacity[38], and enrichment of hypoxia-responsive transcriptional programs across tissues. Together, these findings are consistent with a model of increased ATP turnover and oxygen consumption[42] in fast-growing birds, with liver fulfilling elevated energetic demands primarily through substrate-level pathways rather than mitochondrial oxidative phosphorylation.

Differences in the magnitude of transcript-derived reaction effects and predicted flux changes likely reflect post-transcriptional regulation, allosteric control, and thermodynamic constraints that modulate metabolic activity beyond transcript abundance. Importantly, across all tissues, we did not observe statistically significant cases where transcript-derived reaction effects and predicted flux changes were oppositely directed. This directional concordance indicates that transcriptional regulation provides coherent constraints on the direction of metabolic flux redistribution, while network topology, stoichiometry, and thermodynamic feasibility shape the magnitude of flux responses. Thus, transcript-flux discordance is better interpreted as regulatory amplification or attenuation rather than conflicting regulatory signals, and is consistent with metabolomic profiles that capture buffered steady-state concentrations rather than instantaneous pathway activity.

To quantify flux redistribution in a structured and interpretable manner, we developed reaction-level and metabolite-centered Differential Pathway Flux Analysis (r-DPFA and mc-DPFA) as complementary flux-centric tools, and introduced Transcript-Flux Concordance Analysis (TFCA) to systematically compare transcript-derived reaction effects with model-predicted flux responses at the reaction level. These approaches enable pathway-scale summarization of differential reaction fluxes while localizing changes to specific metabolite hubs that drive system-level reorganization. In addition, gene–protein–reaction-aware concordance analysis allowed systematic aggregation of multi-gene transcriptional effects to the reaction level, facilitating direct comparison with model-predicted flux responses. Given the limited statistical power inherent to metabolomic measurements in this study, we relied on interval-based effect-size statistics[43,44] rather than strict significance thresholds to characterize metabolite-level changes.

Several limitations should be considered when interpreting these results. Sample sizes were modest ($n = 12$ per group), reducing power to detect subtle effects after multiple-testing correction. Although refined here into the *i*ES1470 reconstruction, the original iES1300 model[2] remains incomplete, with several muscle-specific pathways absent from the network. Furthermore, single-tissue models approximate metabolite exchange through boundary constraints rather than explicitly modeling inter-organ circulation, limiting representation of liver–muscle crosstalk[45,46]. Finally, context-specific reconstructions rely on biomass-oriented objective functions, which may not fully capture non-growth metabolic priorities in differentiated tissues.

Several avenues for future development emerge from this work. First, reconstruction of an updated chicken genome-scale metabolic model using current genomic and proteomic resources, potentially seeded from HumanGEM via orthology, would substantially expand pathway coverage. Second, benchmarking alternative context-specific reconstruction methods, such as tINIT within the `troppo` framework, may reduce reliance on biomass-driven objectives while preserving phenotypic anchoring of flux predictions.

## Conclusions

This study examined how genetic variation in growth rate translates into tissue-specific metabolic reprogramming in chickens, testing the hypothesis that fast-growing birds exhibit coordinated, tissue-partitioned metabolic adaptations detectable across flux predictions, transcriptomic programs, and metabolite profiles. Our results support this hypothesis: tissue-specific metabolic strategies emerged consistently across all three omics layers, with directional agreement between transcript-derived reaction effects, predicted flux changes, and metabolite concentration shifts providing convergent evidence for coherent transcriptional constraint on metabolic adaptation.

Fast-growing birds displayed distinct adaptations across tissues: breast muscle relied on amino acid catabolism and one-carbon metabolism for energy provision despite anabolic demands, leg muscle exhibited metabolic flexibility through pathway redistribution with pronounced ketone body and lipid engagement, and liver showed elevated central carbon and amino acid catabolism with reduced oxidative phosphorylation, accompanied by signatures of metabolic stress. Transcriptomic enrichment of hypoxia-response programs and Wnt signaling across muscle tissues, alongside coordinated suppression of cell cycle activity across all three tissues, further reinforced this picture of hypertrophic rather than proliferative growth under conditions of elevated metabolic demand.

The flux-centric tools introduced in this study — reaction-level and metabolite-centred Differential Pathway Flux Analysis (DPFA) — provide a systematic framework for quantification of metabolic alterations across genome-scale networks and enable principled localisation of flux changes to specific metabolite nodes. Transcript-flux concordance analysis (TFCA) further facilitates systematic evaluation of transcript–flux agreement at the reaction level, enabling identification of regulatory events that operate beyond transcriptional control.

From an applied perspective, these findings highlight tissue-specific metabolic trade-offs associated with selection for rapid growth that are not captured by conventional performance metrics[6,7]. The cross-omics consistency observed here suggests that integrative flux-based approaches offer a principled route toward identifying metabolic vulnerabilities relevant to sustainable breeding strategies.

## Methods

### Experimental design

To investigate metabolic differences associated with divergent growth performance, we generated second-generation (F2) cross individuals of chickens by controlled crossbreeding of Russian Snow White (egg-laying) and White Cornish (meat-oriented) breeds with support from the Saint Petersburg Livestock Breeding Center. This F2 resource population has been previously characterized for growth and meat production traits[47], providing a well-established experimental framework for investigating metabolic mechanisms underlying divergent growth performance.

All birds were maintained on the same diet and under identical housing conditions. Rearing was conducted during the cooler autumn-spring period to minimize thermal stress, with facility temperatures kept stable. All husbandry, blood sampling, and euthanasia procedures were performed by licensed personnel at the Federal Research Center for Animal Husbandry named after Academy Member L.K. Ernst in accordance with the applicable national legislation of the Russian Federation governing animal research (Order of the Ministry of Health No. 199n, 2016) and the Center's standard operating procedures. Birds were humanely euthanized by manual cervical dislocation performed by trained personnel. Blood samples were collected immediately prior to euthanasia. Serum was prepared by allowing blood to clot at room temperature for 30–60 minutes, followed by centrifugation at 3000 rpm for 10 minutes at room temperature. Serum samples were then aliquoted and stored at $-80\,^{\circ}$C until analysis. Immediately postmortem, the following tissues were dissected, weighed, snap-frozen in liquid nitrogen, and stored at $-80\,^{\circ}$C: liver (LV), leg muscle (LM), and breast muscle (BM; *pectoralis major*). The present study focuses on these tissues; additional organs were archived for subsequent investigations.

From each of the 12 maternal lineages, two individuals representing the lowest and highest body mass were selected, yielding 12 fast-growing (FG) and 12 slow-growing (SG) chickens (Fig. 7; Supplementary Table 1). Notably, the fast- and slow-growing individuals within each pair were full male siblings from the F2 generation. Thus, any observed metabolic differences could be evaluated against a shared genetic background, thereby minimising the potential confounding influence of inter-individual genetic variation. Detailed information on paternal and grandparental lineages for all subjects is provided in Supplementary Table 1. Within each sibling pair, the fast- and slow-growing individuals differed in mean daily gain (ADG) by more than 20%, with some pairs showing differences exceeding 40% (Supplementary Table 1). This stratified sampling captured the natural extremes of growth variation within the F2 population.

All husbandry, blood sampling, and euthanasia procedures were approved by the LKEFRCAH Commission on the Ethics of Animal Experiments (Protocol No. 3/1, approved 4 December 2019) and conducted in accordance with the applicable national legislation of the Russian Federation (Order of the Ministry of Health No. 199n, 2016). The authors complied with the ARRIVE guidelines in the design and reporting of this study.

### Phenotypic analysis of organ weights and serum biochemistry

We evaluated 40 phenotypic variables: 22 carcass/organ and growth metrics and 18 serum biochemistry indices (Supplementary Table 1). Serum parameters included total protein (g/L), albumin (g/L), globulin (g/L), A/G ratio, creatinine ($\mu$mol/L), glucose (mmol/L), total bilirubin ($\mu$mol/L), triglycerides (mmol/L), cholesterol (mmol/L), ALT (IU/L), AST (IU/L), De Ritis ratio (AST/ALT), calcium (mmol/L), phosphorus (mmol/L), Ca/P ratio, magnesium (mmol/L), iron ($\mu$mol/L), and chloride (mmol/L).

Between-group contrasts (FG compared with SG) were assessed using the Mann-Whitney U test (Wilcoxon rank-sum) with Benjamini-Hochberg FDR control; effect sizes were summarized with Cliff's delta. For descriptive inference, we reported

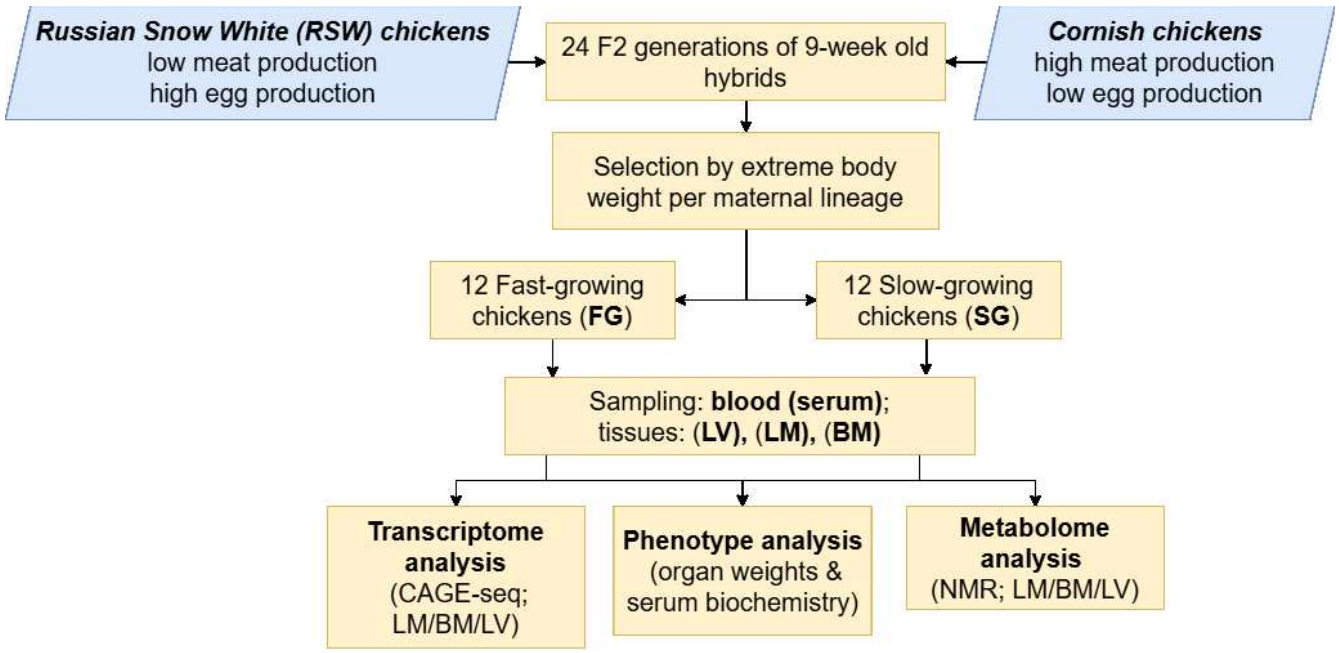



**Figure 7. Overview of the experimental design.**
Crossbreeding of Russian Snow White and White Cornish chickens yielded F2 cross individuals of chickens. At 9 weeks, two individuals per maternal lineage with extreme body weights were selected, forming fast-growing (FG) and slow-growing (SG) groups. Sampling included blood (serum) and three tissues: liver (LV), leg muscle (LM), and breast muscle (BM). These samples were subsequently used for transcriptome (CAGE-seq), phenotypic (organ weights and serum biochemistry), and metabolomic (NMR) analyses.

group medians together with 95% bootstrap confidence intervals (percentile method, $B = 1000$; resampling within groups). Missing values were listwise removed before resampling.

For visualisation, distributions of FDR-significant traits ($p_{adj} < 0.05$) are shown as boxplots. Exploratory multivariate analyses included PCA and PLS-DA to visualise tissue-level structure.

### Metabolomic profiling

Quantitative metabolomic profiling of chicken tissues was performed using proton nuclear magnetic resonance ($^1$H-NMR) spectroscopy. Water-soluble metabolites were extracted from tissue samples following a previously described procedure[48]. Briefly, frozen tissue (approximately 100 mg) was homogenized in cold methanol, then water and chloroform were added at a 2:1:2 ratio (v/v/v). After stirring, the mixture was incubated at $-20\,^{\circ}$C for 30 min and centrifuged at $0\,^{\circ}$C, 13,200 rpm for 30 min to separate phases. The upper water-methanol phase containing polar metabolites was collected and vacuum-dried for analysis. Dried extracts were re-dissolved in deuterated phosphate buffer (50 mM, pH 7.2) containing DSS internal standard (20 μM). $^1$H-NMR measurements were carried out at the Center of Collective Use "Mass spectrometric investigations" SB RAS using an AVANCE III HD 700 MHz NMR spectrometer (Bruker BioSpin, Ettlingen, Germany). A standard pulse sequence with water presaturation and a $70^{\circ}$ detection pulse with 10 s repetition time was used. Final spectra were obtained by summing 64 scans. Metabolite concentrations were measured relative to the DSS internal standard and normalized to wet tissue weight (nmol/g). Phase and baseline corrections and signal integration were performed using MestReNova v.12 software (Mestrelab Research S.L., A Coruña, Spain). Metabolites were identified based on NMR data from the HMDB[49], AMDB[50] databases and an in-house library.

To avoid confounding by tissue-specific metabolic profiles evident from principal component analysis, all analyses were conducted independently within each tissue type (breast muscle, liver, leg muscle). Given the subtle between-group differences relative to within-group variability and the presence of sporadic missing values, robustness was prioritized over parametric efficiency. Between-group differences were estimated using the Hodges-Lehmann (HL) estimator for independent samples[43]:

$$\mathrm{HL} = \mathrm{median}_{i,j}(x_i - y_j), \tag{1}$$

where $x_i$ and $y_j$ denote metabolite concentrations in the FG and SG groups, respectively. This rank-based estimator is less sensitive to outliers than the mean difference and naturally accommodates unbalanced or incomplete data through pairwise

comparisons. Missing values occurred sporadically ($\leq 5\%$ of observations) due to peak overlap or concentrations below detection limits; they were excluded listwise within each metabolite–tissue pair prior to analysis. Effective sample sizes ranged from $n = 8$ to $n = 12$ per group depending on the metabolite.

A biological relevance threshold was defined based on Cohen's "small effect" criterion ($d = 0.2$)[51]. For each metabolite and tissue, the threshold was calculated as:

$$\delta = 0.2 \cdot \left(1.4826 \cdot \mathrm{MAD}_{\mathrm{pooled}}\right), \tag{2}$$

where $\mathrm{MAD} = \mathrm{median}(|z_i - \mathrm{median}(z)|)$ is the median absolute deviation computed on pooled group data, and the factor 1.4826 makes MAD a consistent estimator of the standard deviation under normality. This threshold corresponds to one-fifth of a pooled standard deviation and represents a conservative benchmark for potentially meaningful biological differences in the absence of metabolite-specific clinical anchors.

Confidence intervals (95%) for the HL estimator were obtained using the bias-corrected and accelerated (BCa) bootstrap method[52,53] with $B = 10{,}000$ resamples drawn independently within each group. Let $\mathrm{HL}_1^*, \ldots, \mathrm{HL}_B^*$ denote the HL estimates across bootstrap replicates. Two empirical proportions were computed: $\hat{p}_{\mathrm{dir}}$, the fraction of replicates with $\mathrm{HL}_b^* > 0$ (or $< 0$ for effects in the negative direction), quantifying directional consistency; and $\hat{p}_{\mathrm{mag}}$, the fraction with $|\mathrm{HL}_b^*| > \delta$, quantifying the probability that the effect exceeds the biological relevance threshold.

Decision thresholds were defined a priori. Thresholds $t_{\mathrm{dir}} = 0.85$ and $t_{\mathrm{mag}} = 0.85$ represent the minimum bootstrap proportions yielding interpretable, non-trivial results while maintaining conservative selectivity. The threshold $\alpha_{\mathrm{MW}} = 0.25$ serves as a liberal frequentist gate consistent with the exploratory intent of this analysis and the limited statistical power at $n \approx 10$ per group. A metabolite was considered to show a potentially meaningful difference if all three of the following criteria were simultaneously satisfied:

1. *Directional consistency*: $\hat{p}_{\mathrm{dir}} > t_{\mathrm{dir}} = 0.85$;
2. *Practical magnitude*: $\hat{p}_{\mathrm{mag}} > t_{\mathrm{mag}} = 0.85$;
3. *Frequentist corroboration*: Mann–Whitney $p < \alpha_{\mathrm{MW}} = 0.25$.

This triangulation approach requires convergence of three independent lines of evidence, reducing the likelihood that any single criterion alone drives a finding.

All analyses were performed in Python 3.13[54] using NumPy v1.24[55] and SciPy v1.11[56]. BCa bootstrap intervals used the `bcaboot` package v0.2-1 in R 4.3.2[57] via `rpy2` v3.5[58]. Visualizations were created using Matplotlib v3.7[59] and Seaborn v0.12[60].

## CAGE-seq transcriptome profiling

Transcriptome profiling was performed using CAGE-seq (Cap Analysis Gene Expression) to precisely map transcription start sites (TSS) and quantify promoter activity across four metabolically relevant tissues: breast muscle (BM), heart, leg muscle (LM), and liver (LV). These tissues are central to energy metabolism and endocrine regulation, making them particularly informative for elucidating growth-related mechanisms. All genomic coordinates are reported relative to *GGRsw1* assembly[61].

Total RNA was isolated from sampled tissues using the RNeasy Mini Kit (Qiagen, Hilden, Germany) following the manufacturer's protocol. RNA concentration and purity were assessed using a NanoPhotometer (Implen), while RNA integrity was evaluated with an Agilent 2100 Bioanalyzer (Agilent Technologies, Santa Clara, CA, USA). Libraries were prepared using the nAnT-iCAGE protocol with $5\,\mu g$ of total RNA per sample (nAnT-iCAGE Library Preparation kit DNA form, Yokohama, Japan; SuperScript III Reverse Transcriptase, Invitrogen, Waltham, MA, USA). First-strand cDNA was synthesized and biotinylated at the $5'$ end to enable capture of $5'$-capped mRNA molecules using streptavidin beads (Dynabeads M-270 Streptavidin, Thermo Fisher Scientific, USA). Capped cDNAs were isolated and treated with RNase I/H to remove residual RNA, followed by purification with RNACleanUP (Beckman Coulter, Brea, CA, USA) and ligation to adapters. The second cDNA strand was then synthesized, unique molecular identifiers (UMIs) were incorporated to enable PCR-duplicate detection, and libraries were PCR-amplified.

Sequencing was carried out on the DNBSEQ-G400 platform (MGI) in paired-end mode (PE150), generating approximately $4.5 \times 10^9$ read pairs across all libraries. This sequencing depth enabled robust quantification of both high- and low-abundance transcripts. Raw read quality was assessed with FastQC (v0.11.8)[62]. Several CAGE-specific patterns were observed and deemed compatible with downstream analysis: (i) excess G at read-1 positions 1–2, consistent with template-free activity of reverse transcriptase and potentially introducing 1–2 bp TSS offsets during mapping; (ii) multimodal GC content and higher GC in read-1 compared to read-2, attributable to nucleotide composition near $5'$ transcript ends in chicken; (iii) high sequence duplication levels, reflecting promoter-level saturation for highly expressed genes; and (iv) overrepresented sequences from abundant transcripts such as actin in BM (3.1 %).

Adapter sequences were inferred empirically by paired-end overlap alignment (Needleman-Wunsch algorithm) and found to be consistent across all samples: 3′ adapter AGATCGGAAGAGCACACGTCTGAACTCCAG and 5′ adapter AGATCGGAAGAGCGTCGTGTAGGGAAAGAG. Adapters were detected in 3.7% of reads and removed using AdapterRemoval (v2.3.3)[66] in palindromic mode. Trimmed reads were then aligned to the Russian Snow-White (*GGRsw1*) assembly using STAR (v2.7.9a) with parameters allowing for long introns; only uniquely mapped reads were retained for downstream analyses, yielding a mean unique-mapping rate of 92.3%.

PCR duplicates were identified and removed using the eight-nucleotide UMIs incorporated during library preparation. Deduplication was performed with UMI-tools (v1.1.4)[63] using parameters `--edit-distance-threshold=2 --paired --spliced-is-unique --soft-clip-threshold=1000`. Up to 85% of reads per sample were marked as PCR duplicates and excluded from further analysis, reflecting the expected amplification of highly expressed promoters.

Following deduplication, the 5′ ends of aligned reads were used to identify transcription start sites at single-nucleotide resolution. Because transcription commonly initiates within short promoter regions rather than at discrete positions, 5′ ends were clustered using the DPI1 algorithm. In total, 161,343 TSSs were identified: 152,281 on canonical chromosomes and 9,062 on unplaced contigs, with a median TSS cluster width of 11.9 nucleotides. TSS peaks were annotated by association with gene models from the *GGRsw1* annotation (GTF). Of the 161,343 DPI1 peaks, 101,539 were assigned to known genes while 59,804 represented TSSs of unannotated transcripts. Within the annotated set, 10,860 peaks overlapped annotated gene TSS positions, 55,380 overlapped known exons, 16,101 overlapped introns, and 11,506 and 7,692 were located within 10 kb upstream and downstream of known genes, respectively, representing putative novel TSSs of known genes. Coordinates of TSS peaks (BED/TSV format), per-peak expression values (raw counts and TPM), peak-to-gene assignments, and detailed genomic annotations are available in the CAGE-seq data repository (see Data Availability Statement).

### Gene expression analysis

Differential expression between FG and SG groups was assessed at the gene level using CAGE-seq counts aggregated via the *GGRsw1* peak-to-gene map. Analysis was performed with DESeq2 (v1.42.1)[64] using size-factor normalization, negative-binomial generalized linear models with Wald tests for the FG versus SG contrast, and Benjamini-Hochberg correction for multiple testing.

Gene Set Enrichment Analysis was performed separately for each tissue (BM, LM, LV) using `clusterProfiler` (v4.10.1)[65] with the `gseGO()` function in preranked mode. All genes passing DESeq2's independent filtering were included in the ranked input without additional pre-filtering; genes were ranked by the Wald statistic from the FG versus SG contrast in descending order. Gene sets were obtained from GO Biological Process via `org.Gg.eg.db` (v3.18.0) for *Gallus gallus*, restricted to sets of 15–1,000 genes. Enrichment was estimated using 100,000 gene-set permutations with a permissive collection threshold of $p < 0.25$ and Benjamini-Hochberg FDR correction; terms were retained as significant if $p_{adj} < 0.05$ and $q < 0.05$. For visualization, enriched terms present in at least two tissues are shown in the main figures; tissue-specific terms are provided in Supplementary Table 2.

### Refinement of the *i*ES1300 Genome-Scale Metabolic Model

The published *i*ES1300 genome-scale metabolic model was systematically refined using COBRApy (0.30.0)[67] to improve stoichiometric consistency, annotation completeness, and network connectivity. These refinements ensured thermodynamic feasibility and enabled reliable comparative flux analyses across tissue- and growth-specific context models.

Refinement addressed four core objectives: (i) elimination of stoichiometric inconsistencies through correction of reaction mass and charge balance; (ii) reduction of dead-end metabolites via integration of curated transport reactions; (iii) comprehensive annotation of metabolites and reactions, as the original model lacked metabolite chemical formulas, metabolite database identifiers, and reaction subsystem assignments; and (iv) resolution of energetic inconsistencies identified through MACAW (v1.0.0) diagnostics[68].

Chemical formulas were assigned to all 2,570 metabolites using curated biochemical databases (PubChem, BiGG, MetaNetX, ChEBI). Metabolite and reaction annotations were expanded through systematic mapping to standardized database identifiers. Reaction stoichiometry was corrected to ensure mass and charge conservation. Subsystem classifications were assigned to all reactions to facilitate pathway-level analyses. Pathway annotations were sourced primarily from KEGG[69], with reactions appearing in multiple KEGG pathways annotated accordingly. For reactions absent from KEGG, subsystem assignments were derived from reference reconstructions including Recon3D[70], iCHOv1[71], and iMM1415[72].

Dead-end metabolites in the original model were predominantly compartment-specific entities located in subcellular organelles (e.g. mitochondria, endoplasmic reticulum, peroxisomes, Golgi apparatus, nucleus) lacking intracellular transport to or from the cytosol. In order to enhance connectivity while preserving biological accuracy, the relevant intracellular transport reactions were transferred from HumanGEM, standardised to BiGG-compliant identifiers, and prefixed with `HUMANGEM_` for the purpose of traceability. To prevent introduction of artefactual flux cycles, the expanded transport reaction set was screened

using MACAW-based loop detection, and reactions enabling thermodynamically infeasible loops were removed. Additionally, selected irreversible reactions were constrained based on known thermodynamic directionality (e.g., pyrophosphate hydrolysis).

Model quality was assessed using the Memote (v0.16.1) test suite[73]. The refined model, designated *i*ES1470 (1,470 genes, 2,570 metabolites, 2,698 reactions). This curated reconstruction served as the foundation for all tissue-specific context models and comparative flux analyses.

### Integration of gene expression into the iES1470 GSM using RIPTiDe

The refined model was used to construct context-specific models through the integration of TMM data using RIPTiDe[74]. Flux distributions were compared between these models and analyzed with previously identified DEGs. RIPTiDe adjusts the reaction rates in the metabolic model based on gene expression levels, enabling the generation of context-specific models that reflect the expression patterns of different genes. This process helps simulate the effects of various growth conditions on metabolism and provides insight into active metabolic pathways.

For metabolic modelling, group-level transcript weights were computed as the *median* of TMM-normalised expression across biological replicates (edgeR v4.6.0) to mitigate occasional within-group correlation breakdowns and non-normality. These weights were supplied to RIPTiDe (v3.4.79). Biomass served as the objective function; no reactions were forcibly kept active.

To tune transcript-flux coupling, we varied RIPTiDe's `fraction` from 0.05 to 0.95 in steps of 0.05 for each tissue (LV/LM/BM) and group (FG/SG). For every setting we recorded Spearman's correlation between transcript levels and reaction fluxes (as implemented internally by RIPTiDe), the corresponding $p$-value, and the biomass objective value.

Model selection prioritized transcript-flux concordance while verifying phenotypic consistency. For each tissue and group, we varied RIPTiDe's coupling parameter and ranked models by Spearman correlation between transcript levels and predicted fluxes. The models achieving highest concordance (largest r with $p < 0.05$) were additionally evaluated for phenotypic plausibility by examining the direction of predicted flux through the maintenance ATP reaction (`BIOMASS_maintenance`), which serves as a proxy for cellular energy expenditure in this reconstruction. Models from FG animals consistently exhibited higher predicted maintenance flux relative to SG counterparts across tissues, directionally consistent with the approximately 2-fold higher median organ masses observed in FG animals at 9 weeks. This directional alignment served as phenotypic validation rather than an imposed constraint, confirming that transcript-driven flux predictions captured physiologically relevant differences in cellular energy demand without requiring explicit inter-model coupling within the LP problems.

### Computational analysis of context-specific metabolic models

For each tissue (LV, LM, BM), RIPTiDe-derived models were solved to obtain steady-state flux distributions for FG and SG (linear programming; solver as above). To complement model-level comparison, we applied a custom Pathway Flux Analysis (DPFA) pipeline comprising three components: differential reaction fluxes (DRFs), reaction-level Differential Pathway Flux Analysis (r-DPFA), and metabolite-centered Differential Pathway Flux Analysis (mc-DPFA).

The pathway annotations derived from KEGG[69] and reference models served as the basis for reaction-level classification. Individual pathways were selectively merged into broader subsystems to improve interpretability; pathways with distinct biological roles were retained as separate subsystems. The resulting subsystems comprised: central energy metabolism (citric acid cycle, glycolysis/gluconeogenesis, pyruvate metabolism); oxidative phosphorylation; redox & pentose metabolism (pentose phosphate pathway, pentose and glucuronate interconversions, glutathione metabolism); lipid metabolism (fatty acid biosynthesis, degradation, and general fatty acid metabolism; triacylglycerol synthesis; ketone body synthesis and degradation; cholesterol metabolism; glycerophospholipid metabolism); central amino acid metabolism (alanine/aspartate/glutamate, glycine/serine/threonine, and general amino acid biosynthesis); aromatic amino acid metabolism (tryptophan/phenylalanine/tyrosine); branched-chain amino acid (BCAA) metabolism (valine/leucine/isoleucinebiosynthesis and degradation); other amino acid pathways (cysteine/methionine metabolism, lysine degradation, arginine biosynthesis, proline metabolism); nucleotide metabolism (purine synthesis, pyrimidine synthesis, pyrimidine metabolism, pyrimidine catabolism, nucleotide interconversion); nitrogen disposal (nitrogen metabolism, urea cycle, purine catabolism); folate metabolism; mitochondrial transport; and extracellular transport. This organisation reflects established metabolic relationships in muscle hypertrophy, energy homeostasis, and poultry nitrogen metabolism[75–77].

To focus the analysis on metabolites with interpretable pathway-specific roles, a predefined exclusion list was applied prior to mc-DPFA. Metabolites serving as universal cofactors, currency carriers, or inorganic species were excluded, as their participation in a large number of mechanistically unrelated reactions limits their utility as pathway-specific markers. Excluded species included redox cofactors ($NAD^+$, $NADP^+$), energy currency metabolites (ATP, ADP, AMP), acyl-carrier intermediates (CoA, short-chain acyl-CoA esters), electron transport chain quinones (ubiquinol-10, ubiquinone-10), inorganic ions and small molecules ($H_2O$, $CO_2$, $H^+$, $HPO_4^{2-}$, $PP_i$, $HCO_3^-$), and lipoamide cofactors.

**Notation.** Let $g \in \{FG, SG\}$ denote the group (fast/slow). Let $v_r^{(g)}$ be the steady-state flux of reaction $r$ (mmol $gDW^{-1}$ $h^{-1}$)

in group $g$. For pathway $P$, let $R(P)$ denote the set of reactions annotated to $P$; for metabolite $m$, let $R(m)$ be the set of reactions that either produce or consume $m$.

**Reaction-level Differential Pathway Flux Analysis (r-DPFA)** characterises pathway-level flux redistribution through two complementary measures derived from reaction-level classification and pathway-level flux summation.

As a first step, each reaction was classified into a differential reaction flux (DRF) category by comparing activity between FG and SG:

- **Increased:** flux elevated by more than 20% in FG compared to SG.
- **Decreased:** flux reduced by more than 20% in FG compared to SG.
- **On/Off:** reaction active only in FG (*on*) or only in SG (*off*).
- **Reversed:** opposite net direction between FG and SG.

The 20% threshold was selected to balance sensitivity for detecting biologically meaningful flux changes against specificity, minimizing classification of minor numerical variations as differential regulation. Reactions with absolute flux below $10^{-6}$ mmol gDW$^{-1}$ h$^{-1}$) were treated as inactive (zero flux) for classification purposes.

The total flux through pathway $P$ in group $g$ was computed as the sum of absolute fluxes across all reactions annotated to $P$ (Eq. 3):

$$T_P^{(g)} = \sum_{r \in R(P)} \left| v_r^{(g)} \right|. \tag{3}$$

The between-group total flux shift was defined as $\Delta_P = T_P^{(\mathrm{FG})} - T_P^{(\mathrm{SG})}$. This absolute metric quantifies the net impact of differentially regulated reactions on overall pathway throughput: a large $|\Delta_P|$ driven by few DRF-classified reactions indicates that individual reaction changes carry substantial pathway-level consequence, whereas a small $|\Delta_P|$ despite many DRF-classified reactions indicates compensatory or opposing changes within the pathway. Together, the DRF composition and $\Delta_P$ provide two complementary views—the number and direction of reaction-level changes, and their aggregate effect on pathway flux. A per-reaction normalised metric, $\bar{\Delta}_P = \Delta_P / R(P)$, was additionally computed to facilitate size-adjusted comparison across pathways.

**Metabolite-centered Differential Pathway Flux Analysis (mc-DPFA).** Each metabolite $m$ was linked to pathways via the reactions it participates in. Prior to flux aggregation, metabolite occurrences across compartments were consolidated, such that all reactions involving any compartmental form of $m$ were considered jointly, irrespective of subcellular localisation. For a given metabolite–pathway pair $(m, P)$, only reactions that both involve $m$ and are annotated to $P$ were considered, i.e. the set $R(P) \cap R(m)$. The total flux associated with $m$ within pathway $P$ in group $g$ was calculated according to Eq. 4:

$$T_{m,P}^{(g)} = \sum_{r \in R(P) \cap R(m)} \left| v_r^{(g)} \right|. \tag{4}$$

To quantify between-group differences, we defined the $\log_2$ fold change as shown in Eq. 5:

$$\mathrm{LogFC}_{m,P} = \log_2 \left( \frac{T_{m,P}^{(\mathrm{FG})}}{T_{m,P}^{(\mathrm{SG})}} \right). \tag{5}$$

This value was computed only if both $T_{m,P}^{(\mathrm{FG})}$ and $T_{m,P}^{(\mathrm{SG})}$ exceeded $10^{-6}$ mmol gDW$^{-1}$ h$^{-1}$); otherwise the $(m, P)$ pair was excluded. Metabolite–pathway pairs in which one group had zero turnover (below threshold) while the other did not were assigned a nominal $\mathrm{LogFC}_{m,P}$ of $+6$ (active in FG only) or $-6$ (active in SG only) to represent qualitative on/off metabolic states.

### Transcript-Flux Concordance Analysis (TFCA)

RIPTiDe and related context-specific modeling approaches integrate transcript abundance to predict metabolic flux distributions. These methods typically report global correlations between transcript levels and predicted fluxes as a summary measure of model performance. RIPTiDe calculates Spearman rank correlation coefficients between transcript abundance and median absolute flux values to provide such a benchmark. However, these aggregate metrics have recognized limitations: correlations

are often modest even for well-performing models, and global statistics do not reveal where specific discrepancies occur or whether they are statistically significant at the level of individual reactions.

To complement global concordance measures and address these limitations, we performed a reaction-level concordance analysis that systematically compares transcript-based expectations with model-predicted flux changes.

For each reaction, two independent measures of metabolic change between fast-growing and slow-growing groups were quantified. The *transcript-derived reaction effect* represents the expected change in reaction activity inferred solely from differential gene expression. This metric was computed by aggregating gene-level $\log_2$ fold-changes obtained with DESeq2 through gene–protein–reaction (GPR) mappings. For enzyme complexes requiring multiple subunits (AND logic), the minimum fold-change across required genes was used, reflecting the limiting subunit principle; for reactions catalysed by alternative isoforms (OR logic), the maximum fold-change was taken, assuming dominance of the most strongly expressed isoform. This min/max aggregation rule is consistent with established approaches to mapping transcriptomic data onto GPR associations in constraint-based modeling[78–80]. Statistical significance was propagated to the reaction level by applying intersection–union tests[81] for AND relationships, requiring significance across all subunits, and harmonic mean $p$-value combination[82] for OR relationships, accommodating dependence among isoform-level tests while preserving sensitivity to the strongest individual signal.

The predicted flux change represents the model-derived response after constraint-based optimization and reflects how transcriptional signals are propagated through network topology, stoichiometry, and thermodynamic constraints. Reaction-level flux changes were quantified as $\log_2$ fold-changes in predicted fluxes between RIPTiDe-derived context-specific models for FG and SG. Reactions active in only one condition were assigned fixed values of $+3$ or $-3$ on the $\log_2$ scale to represent qualitative on/off transitions.

To focus on substantial and interpretable regulatory events while maintaining sufficient coverage, concordance analysis was restricted to reactions where the transcript-derived reaction effect exceeded an absolute $\log_2$ threshold of 0.50 and the predicted flux change exceeded an absolute $\log_2$ threshold of 0.50. The transcript threshold captures moderate-to-strong expression changes, while the flux threshold corresponds to the 20% cutoff used in DRF classification, together balancing sensitivity and interpretability.

Discordance between transcript-derived reaction effects and predicted flux changes highlights regulatory mechanisms operating beyond transcriptional control. Cases where transcript-derived effects are strong but predicted flux changes are minimal may reflect post-transcriptional regulation, allosteric control, or metabolite-level constraints buffering flux against transcriptional perturbations. Conversely, reactions exhibiting larger flux changes than transcript-derived effects suggest amplification through network structure or pathway coupling. This reaction-level concordance analysis thus serves both to validate the internal consistency of model predictions and to identify candidate metabolic control points where transcriptional regulation is decoupled from flux behavior.

## Acknowledgements

The authors thank the L.K. Ernst Federal Research Center for Animal Husbandry (LKEFRCAH), where the F2 resource population was established, for their support in conducting the animal experiments and providing tissue samples. The authors also thank Dr. Natalia Zinovieva (Director of LKEFRCAH) for her contribution to the conceptual design of the resource population. The authors thank the Ministry of Science and Higher Education of the Russian Federation for access to the NMR equipment.

## Author contributions statement

VK, OG, FK and IA conceived the study. VK developed the DPFA and TFCA frameworks, performed model curation, metabolic modeling, statistical analysis of phenotypic and metabolomic data, GSEA and DEG analysis, and contributed to the preparation of the manuscript. MK contributed to modeling methodology, FBA analysis, and critical revision of the manuscript. IE performed CAGE-seq data processing and analysis. NO and LY conducted NMR metabolomic profiling and metabolite quantification. ES performed CAGE-seq library preparation and sequencing experiments. NV established the F2 resource population, organized and supervised the animal experiment, and coordinated phenotypic data collection. AV collected and systematized phenotypic data. YT supervised NMR metabolomic profiling and contributed to the data interpretation. OG supervised the transcriptomic analysis, contributed to the acquisition of financial support, manuscript preparation, and reviewed the manuscript. FK supervised bioinformatics analysis, contributed to the acquisition of financial support and reviewed the manuscript. IA supervised metabolic modeling, contributed to the design of the study, and manuscript revision. All authors read and approved the final manuscript.

## Supplementary information

**Supplementary Table 1:** Sample metadata and phenotypic measurements. Individual identifiers, sire and dam identities, grandparental lineage assignments, slaughter dates, ADG-based growth group contrasts, and phenotypic measurements (body weights, organ masses, and serum biochemistry) for 24 $F_2$ male chickens (12 fast-growing, 12 slow-growing). (XLSX)

**Supplementary Table 2:** Gene Set Enrichment Analysis (GSEA) results for GO Biological Process. Significantly enriched GO terms ($p_{adj} < 0.05$) identified across breast muscle (sheet 1), leg muscle (sheet 2), and liver (sheet 3), including normalized enrichment scores (NES), adjusted $p$-values, leading edge genes, and term descriptions. (XLSX)

**Supplementary Table 3:** Reaction modifications in the iES1470 model refinement. Corrected reaction stoichiometries (sheet 1: 44 reactions with revised formulas; original and corrected reaction strings) and HumanGEM-derived intracellular transport reactions (sheet 2: 246 curated transport reactions; reaction ID, reaction formula). (XLSX)

**Supplementary Table 4:** Reaction-level Differential Pathway Flux Analysis (r-DPFA) summary. Pathway-level flux summary for all metabolic subsystems, including total pathway flux per group ($T_P^{(FG)}$, $T_P^{(SG)}$), absolute flux shift ($\Delta_P$), per-reaction normalised flux shift ($\bar{\Delta}_P = \Delta_P/|R(P)|$), pathway size ($|R(P)|$), DRF category counts (Increased/Decreased/On/Off/Reversed/Unchanged), reactions assigned to DRF and flux ratio values for breast muscle (sheet 1), leg muscle (sheet 2), and liver (sheet 3). (XLSX)

**Supplementary Table 5:** Metabolite-centered Differential Pathway Flux Analysis (mc-DPFA) summary. Metabolite turnover $\log_2$ fold-changes across pathways in metabolite-associated flux sums (FG/SG) within metabolic pathways for breast muscle (sheet 1), leg muscle (sheet 2), and liver (sheet 3). Only metabolites with $|\log_2 \mathrm{FC}| > 0.75$ in at least two pathways are shown. (XLSX)

**Supplementary Table 6:** Transcript-flux concordance analysis. Reaction-level transcript-derived effects, predicted flux changes, statistical significance, and pathway assignments for breast muscle (sheet 1), leg muscle (sheet 2), and liver (sheet 3). (XLSX)

## Additional information

**Funding:** The study was supported by the grant from the Government of the Russian Federation (25-075-60608-1-0073-000129) No. 075-15-2025-484 29.05.2025 “Post-genomic technologies for poultry production”.

**Competing interests:** The authors declare that they have no competing interests.

**Data availability:** The datasets supporting the conclusions of this article are available in the Avian Metabolome Database repository, https://amdb.online/amdb/experiments/302/. Transcriptomics (CAGE-seq) data are deposited in NCBI GEO under accession number GSE328084 (https://www.ncbi.nlm.nih.gov/geo/query/acc.cgi?acc=GSE328084) and with additional files available at https://chicken.biouml.org/en. The refined iES1470 genome-scale model, RIPTiDe configurations, and DPFA analysis scripts are available via https://github.com/Rimmi-K/chkn26 (archived at https://doi.org/10.5281/zenodo.19095394).

## References

1. Esvelt, K. M. & Wang, H. H. Genome-scale engineering for systems and synthetic biology. *Mol. systems biology* **9**, 641 (2013).
2. Salehabadi, E., Motamedian, E. & Shojaosadati, S. A. Reconstruction of a generic genome-scale metabolic network for chicken: Investigating network connectivity and finding potential biomarkers. *PLOS ONE* **17**, e0254270, DOI: 10.1371/journal.pone.0254270 (2022).
3. Volyanskaya, A. R. *et al.* A bird’s-eye overview of molecular mechanisms regulating feed intake in chickens—with mammalian comparisons. *Animal Nutr.* **17**, 61–74, DOI: 10.1016/j.aninu.2024.01.008 (2024).
4. Volkova, S., Matos, M. R. A., Mattanovich, M. & Marín de Mas, I. Metabolic modelling as a framework for metabolomics data integration and analysis. *Metabolites* **10**, 303, DOI: 10.3390/metabo10080303 (2020).
5. Åkesson, M., Förster, J. & Nielsen, J. Integration of gene expression data into genome-scale metabolic models. *Metab. engineering* **6**, 285–293 (2004).
6. Rauw, W. M., Kanis, E., Noordhuizen-Stassen, E. N. & Grommers, F. J. Undesirable side effects of selection for high production efficiency in farm animals: a review. *Livest. Prod. Sci.* **56**, 15–33, DOI: 10.1016/S0301-6226(98)00147-X (1998).
7. Julian, R. J. Production and growth related disorders and other metabolic diseases of poultry–a review. *The Vet. J.* **169**, 350–369 (2005).
8. Maharjan, P. *et al.* Review: Physiological growth trend of current meat broilers and dietary protein and energy management approaches for sustainable broiler production. *Animal* **15**, 100284, DOI: 10.1016/j.animal.2021.100284 (2021).

9. Nicol, C., Abeyesinghe, S. & Chang, Y.-M. An analysis of the welfare of fast-growing and slower-growing strains of broiler chicken. *Front. Animal Sci.* **5**, 1374609, DOI: 10.3389/fanim.2024.1374609 (2024).

10. Lara, L. J. & Rostagno, M. H. Impact of heat stress on poultry production. *Animals* **3**, 356–369, DOI: 10.3390/ani3020356 (2013).

11. Brugaletta, G., Teyssier, J.-R., Rochell, S. J., Dridi, S. & Sirri, F. A review of heat stress in chickens. part i: Insights into physiology and gut health. *Front. Physiol.* **13**, 934381, DOI: 10.3389/fphys.2022.934381 (2022).

12. Gonzalez-Rivas, P. *et al.* Impact of heat stress on growth performance and carcass traits of fast-, medium- and slow-growing broiler chicken genotypes. *Poult. Sci.* **104**, 104570, DOI: 10.1016/j.psj.2024.104570 (2025).

13. Apalowo, O. O., Ekunseitan, D. A. & Fasina, Y. O. Impact of heat stress on broiler chicken production. *Poultry* **3**, 107–128 (2024).

14. Baghbanzadeh, A. & Decuypere, E. Ascites syndrome in broilers: Physiological and nutritional perspectives. *Avian Pathol.* **37**, 117–126, DOI: 10.1080/03079450801902062 (2008).

15. Alnahhas, N., Pouliot, E. & Saucier, L. The hypoxia-inducible factor 1 pathway plays a critical role in the development of breast muscle myopathies in broiler chickens: a comprehensive review. *Front. Physiol.* **14**, 1260987 (2023).

16. Greene, E., Chen, J., Walk, C., Bedford, M. & Dridi, S. Mitochondrial dysfunction is a hallmark of woody breast myopathy in broiler chickens. *Front. Physiol.* **16**, 1543788, DOI: 10.3389/fphys.2025.1543788 (2025).

17. Zhang, X., Noel, S., Bhatt, D. *et al.* Integrative transcriptomic and metabolomic analysis reveals alterations in energy metabolism and mitochondrial functionality in broiler chickens with wooden breast. *Sci. Reports* **13**, 4747, DOI: 10.1038/s41598-023-31429-7 (2023).

18. Ferretti, A. *et al.* Lipid metabolism analysis in liver of different chicken genotypes and impact on nutritionally relevant polyunsaturated fatty acids of meat. *Sci. Reports* **12**, 1888, DOI: 10.1038/s41598-022-05986-2 (2022).

19. Kikusato, M. & Toyomizu, M. Characterization of mitochondrial content and respiratory capacities of broiler chicken skeletal muscles with different muscle fiber compositions. *Animals* **9**, 527, DOI: 10.3390/ani9080527 (2019).

20. Zaefarian, F., Abdollahi, M., Cowieson, A. & Ravindran, V. Avian liver: The forgotten organ. *Animals* **9**, 63, DOI: 10.3390/ani9020063 (2019).

21. Scheuermann, G. N., Bilgili, S. F. & Hess, J. B. Breast muscle development in commercial broiler chickens. *Poult. Sci.* **83**, 153–158, DOI: 10.1093/ps/83.1.153 (2004).

22. Weng, K. *et al.* Fiber characteristics and meat quality of different muscular tissues from slow- and fast-growing broilers. *Poult. Sci.* **101**, 101537, DOI: 10.1016/j.psj.2021.101537 (2022).

23. Selle, P., de Paula Dorigam, J., Chrystal, P. & Liu, S. A reappraisal of amino acids in broiler chicken nutrition. *World's Poult. Sci. J.* DOI: 10.1080/00439339.2023.2234342 (2023).

24. Dransfield, E. & Sosnicki, A. Relationship between muscle growth and poultry meat quality. *Poult. science* **78**, 743–746 (1999).

25. Scanes, P. Perspectives on the endocrinology of poultry growth and metabolism. *Gen. Comp. Endocrinol.* **163**, 24–32 (2009).

26. Brunk, E. *et al.* Recon3d enables a three-dimensional view of gene variation in human metabolism. *Nat. Biotechnol.* **36**, 272–281, DOI: 10.1038/nbt.4072 (2018).

27. Kim, S. *et al.* PubChem 2019 update: improved access to chemical data. *Nucleic Acids Res.* **47**, D1102–D1109, DOI: 10.1093/nar/gky1033 (2019).

28. King, Z. A. *et al.* BiGG Models: A platform for integrating, standardizing and sharing genome-scale models. *Nucleic Acids Res.* **44**, D515–D522, DOI: 10.1093/nar/gkv1049 (2016).

29. Moretti, S., Tran, V. D. T., Mehl, F., Ibberson, M. & Pagni, M. MetaNetX/MNXref: unified namespace for metabolites and biochemical reactions in the context of metabolic models. *Nucleic Acids Res.* **49**, D570–D574, DOI: 10.1093/nar/gkaa992 (2021).

30. Hastings, J. *et al.* ChEBI in 2016: Improved services and an expanding collection of metabolites. *Nucleic Acids Res.* **44**, D1214–D1219, DOI: 10.1093/nar/gkv1031 (2016).

31. Overbeek, R. *et al.* The SEED and the rapid annotation of microbial genomes using subsystems technology (RAST). *Nucleic Acids Res.* **42**, D206–D214, DOI: 10.1093/nar/gkt1226 (2014).

**32.** Karp, P. D. *et al.* The BioCyc collection of microbial genomes and metabolic pathways. *Briefings Bioinforma.* **22**, bbz134, DOI: 10.1093/bib/bbz134 (2021).

**33.** Lieven, C. *et al.* Memote for standardized genome-scale metabolic model testing. *Nat. Biotechnol.* **38**, 272–276 (2020).

**34.** Gevorgyan, A., Poolman, M. G. & Fell, D. A. Detection of stoichiometric inconsistencies in biomolecular models. *Bioinformatics* **24**, 2245–2251 (2008).

**35.** Wilson, D. F. & Matschinsky, F. M. Metabolic homeostasis in life as we know it: its origin and thermodynamic basis. *Front. physiology* **12**, 658997 (2021).

**36.** Memme, J. M., Erlich, A. T., Phukan, G. & Hood, D. A. Exercise and mitochondrial health. *The J. Physiol.* **599**, 803–817 (2021).

**37.** Hoppeler, H., Baum, O., Lurman, G. & Mueller, M. Molecular mechanisms of muscle plasticity with exercise. *Compr. Physiol.* **1**, 1883–1909 (2008).

**38.** Trefts, E., Williams, A. S. & Wasserman, D. H. Exercise and the regulation of hepatic metabolism. *Prog. molecular biology translational science* **135**, 203–225 (2015).

**39.** Burgess, S. C. *et al.* Elevated tca cycle function in the pathology of diet-induced hepatic insulin resistance and fatty liver. *J. Lipid Res.* **47**, 1073–1081 (2012).

**40.** Perry, C. G. *et al.* Mitochondrial creatine kinase activity and phosphate shuttling are acutely regulated by exercise in human skeletal muscle. *The J. Physiol.* **591**, 5911–5921 (2013).

**41.** Porter, C., Reidy, P. T., Bhattarai, N., Sidossis, L. S. & Rasmussen, B. B. Resistance exercise training alters mitochondrial function in human skeletal muscle. *Medicine Sci. Sports Exerc.* **47**, 1922 (2015).

**42.** Baker, J. S., McCormick, M. C. & Robergs, R. A. Interaction among skeletal muscle metabolic energy systems during intense exercise. *J. nutrition metabolism* **2010**, 905612 (2010).

**43.** Hodges, J. L. J. & Lehmann, E. L. Estimates of location based on rank tests. *The Annals Math. Stat.* **34**, 598–611, DOI: 10.1214/aoms/1177704172 (1963).

**44.** Efron, B. & Tibshirani, R. J. *An Introduction to the Bootstrap* (Chapman & Hall/CRC, Boca Raton, 1994).

**45.** Felig, P. The glucose-alanine cycle. *Metabolism* **22**, 179–207 (1973).

**46.** Graham, T. E. & MacLean, D. A. Alanine and glutamine synthesis and release from skeletal muscle: I. glycolysis and tricarboxylic acid cycle intermediate effects. *Am. J. Physiol. Metab.* **282**, E593–E600 (2002).

**47.** Volkova, N. A. *et al.* Genome-wide association study reveals the genetic architecture of growth and meat production traits in a chicken f2 resource population. *Genes* **15**, 1246, DOI: 10.3390/genes15101246 (2024).

**48.** Tsentalovich, Y. P., Zelentsova, E. A., Yanshole, L. V., Yanshole, V. V. & Odud, I. M. Most abundant metabolites in tissues of freshwater fish perch (perca fluviatilis). *Sci. Reports* **10**, 17128, DOI: 10.1038/s41598-020-73895-3 (2020).

**49.** Wishart, D. S. *et al.* Hmdb 5.0: the human metabolome database for 2022. *Nucleic Acids Res.* **50**, D622–D631, DOI: 10.1093/nar/gkab1062 (2022).

**50.** Yanshole, V. V. *et al.* Animal metabolite database: Metabolite concentrations in animal tissues and convenient comparison of quantitative metabolomic data. *Metabolites* **13**, 1088, DOI: 10.3390/metabo13101088 (2023).

**51.** Cohen, J. *Statistical Power Analysis for the Behavioral Sciences* (Lawrence Erlbaum Associates, 1988), 2nd edn.

**52.** Efron, B. Better bootstrap confidence intervals. *J. Am. Stat. Assoc.* **82**, 171–185, DOI: 10.1080/01621459.1987.10478410 (1987).

**53.** DiCiccio, T. J. & Efron, B. Bootstrap confidence intervals. *Stat. Sci.* **11**, 189–228, DOI: 10.1214/ss/1032280214 (1996).

**54.** Python Software Foundation. Python programming language, version 3.13. https://www.python.org (2024).

**55.** Harris, C. R. *et al.* Array programming with numpy. *Nature* **585**, 357–362, DOI: 10.1038/s41586-020-2649-2 (2020).

**56.** Virtanen, P. *et al.* SciPy 1.0: fundamental algorithms for scientific computing in python. *Nat. Methods* **17**, 261–272, DOI: 10.1038/s41592-019-0686-2 (2020).

**57.** R Core Team. *R: A Language and Environment for Statistical Computing*. R Foundation for Statistical Computing, Vienna, Austria (2023).

**58.** Gautier, L. rpy2: Python interface to the r language. https://rpy2.github.io (2023). Version 3.5.

**59.** Hunter, J. D. Matplotlib: A 2d graphics environment. *Comput. Sci. & Eng.* **9**, 90–95, DOI: 10.1109/MCSE.2007.55 (2007).

**60.** Waskom, M. L. seaborn: statistical data visualization. *J. Open Source Softw.* **6**, 3021, DOI: 10.21105/joss.03021 (2021).

**61.** Yevshin, I. S. *et al.* Genome of russian snow-white chicken reveals genetic features associated with adaptations to cold and diseases. *Int. J. Mol. Sci.* **25**, 11066 (2024).

**62.** Andrews, S. FastQC: A quality control tool for high throughput sequence data (2010). Babraham Bioinformatics, Babraham Institute, Cambridge, United Kingdom.

**63.** Smith, T., Heger, A. & Sudbery, I. Umi-tools: Modeling sequencing errors in unique molecular identifiers to improve quantification accuracy. *Genome Res.* **27**, 491–499, DOI: 10.1101/gr.209601.116 (2017).

**64.** Love, M., Anders, S., Huber, W. *et al.* Differential analysis of count data–the deseq2 package. *Genome Biol* **15**, 10–1186 (2014).

**65.** Wu, T. *et al.* clusterProfiler 4.0: A universal enrichment tool for interpreting omics data. *The Innov.* **2**, 100141, DOI: 10.1016/j.xinn.2021.100141 (2021).

**66.** Schubert, M., Lindgreen, S. & Orlando, L. Adapterremoval v2: Rapid adapter trimming, identification, and read merging. *BMC Res. Notes* **9**, 88, DOI: 10.1186/s13104-016-1900-2 (2016).

**67.** Ebrahim, A., Lerman, J. A., Palsson, B. O. & Hyduke, D. R. Cobrapy: Constraints-based reconstruction and analysis for python. *BMC Syst. Biol.* **7**, 74, DOI: 10.1186/1752-0509-7-74 (2013).

**68.** Moyer, D. C., Reimertz, J., Segrè, D. & Fuxman Bass, J. I. Macaw: a method for semi-automatic detection of errors in genome-scale metabolic models. *Genome Biol.* **26**, 79 (2025).

**69.** Kanehisa, M. & Goto, S. KEGG: Kyoto encyclopedia of genes and genomes. *Nucleic Acids Res.* **28**, 27–30, DOI: 10.1093/nar/28.1.27 (2000).

**70.** Brunk, E. *et al.* Recon3d enables a three-dimensional view of gene variation in human metabolism. *Nat. Biotechnol.* **36**, 272–281, DOI: 10.1038/nbt.4072 (2018).

**71.** Hefzi, H. *et al.* A consensus genome-scale reconstruction of chinese hamster ovary cell metabolism. *Cell Syst.* **3**, 434–443, DOI: 10.1016/j.cels.2016.10.020 (2016).

**72.** Sigurdsson, M. I., Jamshidi, N., Steingrimsson, E., Thiele, I. & Palsson, B. Ø. A detailed genome-wide reconstruction of mouse metabolism based on human Recon 1. *BMC Syst. Biol.* **4**, 140, DOI: 10.1186/1752-0509-4-140 (2010).

**73.** Lieven, C. *et al.* Memote for standardized genome-scale metabolic model testing. *Nat. Biotechnol.* **38**, 272–276, DOI: 10.1038/s41587-020-0446-y (2020).

**74.** Jenior, M. L., Moutinho, T. J., Dougherty, B. V. & Papin, J. A. Transcriptome-guided parsimonious flux analysis improves predictions with metabolic networks in complex environments. *PLOS Comput. Biol.* **16**, e1007099, DOI: 10.1371/journal.pcbi.1007099 (2020).

**75.** Hargreaves, M. & Spriet, L. L. Skeletal muscle energy metabolism during exercise. *Nat. Metab.* **2**, 817–828 (2020).

**76.** Beauclercq, S. *et al.* Muscle transcriptome analysis reveals molecular pathways and biomarkers involved in extreme ultimate ph and meat defect occurrence in chicken. *Sci. Reports* **7**, 6447 (2017).

**77.** He, W., Li, P. & Wu, G. Amino acid nutrition and metabolism in chickens. In *Amino acids in nutrition and health: Amino acids in the nutrition of companion, zoo and farm animals*, 109–131 (Springer, 2021).

**78.** Pacheco, M. P. *et al.* Integrated metabolic modelling reveals cell-type specific epigenetic control points of the macrophage metabolic network. *BMC Genomics* **16**, 809, DOI: 10.1186/s12864-015-1984-4 (2015).

**79.** Ravi, S. *et al.* $\delta$fba—predicting metabolic flux alterations using genome-scale metabolic models and differential transcriptomic data. *PLoS Comput. Biol.* (2017).

**80.** Heirendt, L. *et al.* Creation and analysis of biochemical constraint-based models using the cobra toolbox v.3.0. *Nat. Protoc.* (2019).

**81.** Berger, R. L. Multiparameter hypothesis testing and acceptance sampling. *Technometrics* (1982).

**82.** Wilson, D. J. The harmonic mean p-value for combining dependent tests. *Proc. Natl. Acad. Sci.* **116**, 1195–1200, DOI: 10.1073/pnas.1814092116 (2019).

## Supplementary Files

This is a list of supplementary files associated with this preprint. Click to download.

- S3Table.xlsx
- S4Table.xlsx
- S2Table.xlsx
- S6Table.xlsx
- S5Table.xlsx
- S1Table.xlsx